Novel insights into deep groundwater exploration by geophysical estimation of hard rock permeability

Muhammad Hasan [1, 2, 3,*], **Lijun Su** [1, 2, 3, **]

[1] *State Key Laboratory of Mountain Hazards and Engineering Resilience, Institute of Mountain Hazards and Environment, Chinese Academy of Sciences, Chengdu 610299, China*

[2] *China-Pakistan Joint Research Center on Earth Sciences, CAS-HEC, Islamabad, Pakistan*

[3] *University of Chinese Academy of Sciences, Beijing 100049, China*

*Corresponding authors:

Muhammad Hasan: Email: mhasan@imde.ac.cn; ORCID: https://orcid.org/0000-0001-6804-7962; Phone Number: +86-13051361710

Lijun Su: Email: sulijun1976@163.com; ORCID: https://orcid.org/0000-0001-9972-4698

Corresponding authors' postal address: State Key Laboratory of Mountain Hazards and Engineering Resilience, Institute of Mountain Hazards and Environment, Chinese Academy of Sciences, Chengdu 610299, China

Abstract

Deep groundwater exploration in hard rock terrains is essential in regions with the potential for deep aquifers, especially where water scarcity threatens sustainable development and long-term water security. However, such exploration remains a global challenge due to the geological complexity and the limitations of traditional investigation methods. Accurate estimation of hydraulic parameters, particularly permeability (k), is vital for effective groundwater management and reliable prediction of future scenarios. Conventionally, permeability is measured through borehole investigations. While widely adopted, these methods are intrusive, expensive, time-consuming, and limited to point-scale measurements. Their effectiveness is often restricted to areas with relatively uniform geological settings, and they are generally inadequate for assessing deep groundwater systems. In contrast, geophysical methods offer a non-invasive, cost-effective, and efficient alternative, enabling large-scale assessment of subsurface hydrogeological conditions with minimal surface disruption. Previous geophysical studies have employed empirical approaches, particularly vertical electrical sounding (VES), to estimate permeability. However, these methods are confined to shallow depths, homogeneous settings, and one dimensional interpretation, making them insufficient for application in highly heterogeneous hard rock environments. This study introduces, for the first time, the use of controlled-source audio-frequency magnetotellurics (CSAMT) to estimate two and three dimensional permeability distributions at depths exceeding 1 km in complex geological settings, including sedimentary, igneous, and metamorphic rocks. The results demonstrate that CSAMT can effectively characterize deep subsurface variability and generate accurate, spatially continuous hydrogeological models in hard rock terrains, particularly where drilling data are limited or unavailable. Our approach cuts down on the need for costly borehole tests and allows

for a more thorough assessment of aquifer potential. This research provides a major breakthrough in deep groundwater investigation and helps with better scientific planning and long-term groundwater resource management in challenging hard rock areas.

Keywords: Permeability; Geophysical methods; Hydraulic parameters; Groundwater; Hard rock; Hydrogeological models

1 Introduction

Metamorphic and igneous rocks make up the majority of Earth's crust, covering roughly one-third of the planet's surface (Amiotte Suchet et al., 2003). Research on groundwater in hard rock terrains primarily aims to delineate subsurface geological features, such as fault systems and fracture networks, which are essential for understanding groundwater occurrence and movement (Fernando and Pacheco, 2015; Hasan et al., 2021). A crucial parameter in these studies is aquifer potential, which refers to the ability of rock formations to store and transmit water. This parameter is essential for the monitoring and evaluation of groundwater resources (Majumdar and Das, 2011; Nwosu et al., 2013; Qian et al., 2024). The aquifer potential is influenced by various geological and environmental factors, such as lithology, structural configuration, fault and joint density, mineralogical composition, weathering degree, and water infiltration depth (Dell'Oca et al., 2020; Abbas et al., 2022). Accurately characterizing the lateral and vertical heterogeneity of aquifer properties within complex and massive rock units remains one of the primary challenges in hard rock hydrogeology (Courtois et al., 2010; Dewandel et al., 2006). A thorough assessment of aquifer potential is particularly important in geologically varied environments, where conventional methods frequently prove inadequate due to the complexity of subsurface formations and the scarcity of direct data (Robinson et al., 2016; Worthington et al.,

2016; Zhu et al., 2017). These uncertainties often lead to inefficient or unsustainable groundwater development, worsening water scarcity and environmental degradation (Dewandel et al., 2006; Refsgaard et al., 2012; Lachassagne et al., 2021). Refining cost-effective and reliable methods for assessing subsurface hydrogeological conditions is a fundamental challenge in the study and management of hard rock aquifers.

Groundwater at depths greater than 500 m is typically less affected by surface hydrological processes and frequently contains brackish or saline water (Gleeson et al., 2016; Margat and van der Gun, 2013; Ferguson et al., 2023). Its exploration is increasingly recognized as strategically important in certain geological and environmental contexts. In the Jinji region (study area), various site-specific factors require a targeted examination of these deeper reserves. First, surface water availability is both scarce and unreliable, increasing the importance of deep aquifers as a potential supplementary source of freshwater. Second, the shallow subsurface is largely composed of fresh granite, a rock type known for its inherently low porosity and permeability, thus offering limited groundwater potential (Dewandel et al., 2006; Lachassagne et al., 2021). In contrast, favorable water-bearing zones such as fractured granite, sandstone, and hornstone are typically found at much greater depths. Third, recent national water initiatives in China have underscored the need for deep subsurface exploration, especially in structurally complex terrains, to uncover underutilized aquifers that could contribute to more resilient water supply systems in the face of increasing demand and climatic uncertainties (MOHURD, 2021; Qian et al., 2024). Comprehensive assessments of deep groundwater are therefore essential for identifying these hidden but strategically valuable water sources, evaluating their recharge characteristics, and integrating them into sustainable long-term management plans (Courtois et al., 2010; Refsgaard et al., 2012). As pressures on surface and shallow subsurface water sources

intensify, deeper aquifer systems may serve as a critical buffer, ensuring more reliable water access amid growing environmental and socio-economic challenges.

Multiple studies have recorded the swift depletion of global groundwater reserves, underscoring an increasing concern for water sustainability (Rodell et al., 2009; Wada et al., 2010; Laghari et al., 2012; Jasechko et al., 2024). In light of this significant issue, thorough and precise assessments of groundwater resources are crucial for their effective management and sustainable utilization. A comprehensive understanding of hydraulic properties is essential for these assessments. Permeability is a crucial parameter for characterizing the ability of geological formations to store and transmit water. This factor is crucial for aquifer analysis in various hydrogeological contexts globally (Dewandel et al., 2006; Gerke et al., 2011; Allègre et al., 2016; Fiandaca et al., 2018; Mudunuru et al., 2022; Esmaeilpour et al., 2023; Yan et al., 2024; Carbillet et al., 2024). The aquifer potential of geological layers is usually determined by permeability (Zhang et al., 2004; Pellet et al., 2024). De Lima and Niwas (2000), Soupios et al. (2007), Hasan et al. (2021), and Yang and Zhang (2024) all state that borehole testing is the standard method for measuring aquifer parameters. While boreholes contribute valuable geological data, generating a comprehensive 2D analysis through drilling alone is often time-consuming and challenging (Hubbard and Rubin, 2002; Niwas and De Lima, 2003). Borehole methods are limited by high costs, time-intensive procedures, bulky equipment requirements, and challenging deployment in rugged terrain, while also providing only localized data with limited capability to image lateral and deep subsurface structures (Singh, 2005; Lin et al., 2018; Asfahani, 2023). Uncertainty in groundwater resource estimation can arise from the limited availability of borehole data, as the constraints of drilling make it difficult to conduct frequent and widespread borehole investigations. Alternatively, it is essential to develop methods that minimize the

reliance on costly drilling while still enabling accurate evaluation of groundwater storage capacity within prospective rock formations.

A diverse range of groundwater studies has effectively incorporated geophysical methods to improve subsurface characterization (Bentley and Gharibi, 2004; Yadav and Singh, 2007; Fu et al., 2013; Vouillamoz et al., 2014; Robinson et al., 2016; Lin et al., 2018; Abbas et al., 2022; Kouadio et al., 2023; Zhang et al., 2024). These methods provide notable benefits compared to traditional drilling, especially regarding cost-efficiency, rapid deployment, minimal environmental impact, and ease of field implementation (Hu et al., 2013; Lin et al., 2018; Di et al., 2020; Fusheng et al., 2022; Hasan and Shang, 2022). Geophysical tools offer significant practical advantages, including strong vertical and lateral imaging capabilities, which enhance their effectiveness in capturing the hydrogeological complexity of diverse subsurface conditions (Niwas and De Lima, 2003; Fu et al., 2013; Hasan et al., 2021; Wynn et al., 2016; Kouadio et al., 2023). Resistivity-based methods are pivotal in contemporary groundwater exploration, owing to their sensitivity to diverse subsurface conditions and materials (Bentley and Gharibi, 2004; Camporese et al., 2011; Robinson et al., 2016). The main methods in this category are vertical electrical sounding (VES), electrical resistivity tomography (ERT), and controlled-source audio-frequency magnetotellurics (CSAMT) (Soupios et al., 2007; Di et al., 2020; Zhang et al., 2024). VES has been utilized for one dimensional profiling, especially in areas with horizontally layered aquifers (Niwas and De Lima, 2003; Soupios et al., 2007; Majumdar and Das, 2011; Nwosu et al., 2013; Hasan et al., 2021; Asfahani, 2023). This method is particularly appropriate for small-scale applications (less than 200 m depth), providing low operational costs and reduced logistical requirements. However, its lateral resolution is limited, and its performance can be compromised in geologically complex settings with highly resistive or conductive layers. ERT, by contrast,

enables two and three dimensional imaging up to intermediate depths (~300 m) with significantly improved resolution. It is particularly effective for characterizing complex geological settings, such as fractured zones or karst systems, and is widely used for detailed assessments of aquifer geometry and contamination (Bentley and Gharibi, 2004; Camporese et al., 2011; Lin et al., 2018; Abbas et al., 2022; Hasan and Shang, 2022). Nonetheless, it requires greater field effort, careful electrode spacing, and, like VES, may encounter challenges in highly resistive or conductive environments. CSAMT, a more advanced method, is ideally suited for deep investigations (hundreds to thousands of meters), especially in hard rock terrains. It provides two and three dimensional subsurface imaging with strong sensitivity to deep conductive structures, making it highly effective for delineating deep-seated aquifers and geothermal systems (Smith and Booker, 1991; Simpson and Bahr, 2005; Bai et al., 2010; Fu et al., 2013; Hu et al., 2013; Wang et al., 2015; Wynn et al., 2016; Zhang et al., 2021; Kouadio et al., 2023). While CSAMT typically offers lower spatial resolution than ERT, it excels in deep structural mapping, performs well in areas with high cultural noise due to its controlled-source signals, and can be further enhanced when integrated with empirical or model-based approaches (Zonge and Hughes, 1988; An et al., 2016; Hasan et al., 2025). The choice among these resistivity techniques depends on various factors, including investigation depth, target resolution, geological complexity, logistical constraints, cost, field conditions, and resistivity contrast (Di et al., 2020; Hasan and Shang, 2022). Given these considerations, particularly the need to investigate deep aquifer systems in hard rock environments, CSAMT was determined to be the most suitable method for the present study.

In fractured rock environments, including granitic, metamorphic, and sandstone formations, fluid movement is primarily influenced by the arrangement and connectivity of

fractures, rather than the inherent porosity of the rock matrix. A precise assessment of hydraulic behavior in these environments necessitates the application of integrated methodologies. Recent studies emphasize the necessity of integrating geophysical and hydrogeological methods to accurately identify and characterize hydraulic properties (McKeown et al., 1999; Medici et al., 2023). Interdisciplinary approaches are crucial for improving the precision of flow modeling and for guiding groundwater management and geo-energy development in structurally complex terrains. Resistivity-based methods are essential in groundwater investigations for their ability to delineate subsurface structures and identify areas with water-bearing potential. Recent hydrogeophysical studies have focused on the correlation between electrical resistivity and permeability, as both are closely related to the fluid content and physical structure of subsurface materials. Electrical resistivity, which reflects a material's resistance to the flow of electrical current, is influenced by various factors. These include rock type, porosity, weathering extent, connectivity of the pore network, saturation level, structural features like faults and fractures, and the salinity of pore fluids. Numerous parameters significantly affect permeability, highlighting the utility of resistivity measurements as indicators for evaluating groundwater flow potential (Singh, 2005; Sinha et al., 2009; Hasan et al., 2021). Numerous studies have investigated empirical and semi-empirical correlations between these two parameters, with the objective of utilizing resistivity as a proxy for estimating hydraulic conductivity or permeability in regions with limited data (De Lima and Niwas, 2000; Hubbard and Rubin, 2002; Niwas and De Lima, 2003; Singh, 2005; Soupios et al., 2007; Jardani et al., 2007; Sinha et al., 2009; Majumdar and Das, 2011; Nwosu et al., 2013; Hasan et al., 2021; Asfahani, 2023). Niwas and De Lima (2003) developed an analytical model linking formation resistivity to transmissivity in porous media. Similarly, Jardani et al. (2007) demonstrated the feasibility of employing geophysical inversions

to infer permeability distributions in heterogeneous aquifers. Recent studies have applied these approaches to fractured and hard-rock environments; however, such correlations are less common and frequently constrained by site-specific geological variability (Soupios et al., 2007; Hasan et al., 2021; Asfahani, 2023). Despite recent advancements, the development of robust, high-resolution 2D and 3D permeability models from resistivity data, particularly in geologically complex environments at significant depths, remains a major challenge. To date, no previous studies have successfully achieved this, underscoring the critical need for improved integration of geophysical measurements with sparse borehole data. The relationship between resistivity measurements and borehole-derived data provides an efficient and cost-effective method for estimating aquifer properties over extensive spatial areas and varied depth profiles. This study, for the first time, demonstrates a novel application of the CSAMT technique to create high-resolution two and three dimensional permeability models reaching depths of around 1300 m in a geologically complex and heterogeneous environment characterized by sandstone, granite, and hornstone. A selected number of boreholes were strategically drilled at critical points within the study area. Following this, several CSAMT survey lines were conducted, encompassing both the borehole locations and their surrounding zones. By linking resistivity data from the CSAMT surveys with permeability measurements obtained from borehole core testing, we derived a reliable empirical relationship between resistivity and permeability. This correlation was then applied throughout the entire CSAMT dataset, allowing for the generation of detailed 2D and 3D permeability models even in regions lacking direct borehole data. The method provides a cost-effective and comprehensive framework for evaluating deep groundwater potential, significantly minimizing the reliance on extensive and expensive drilling operations.

This study introduces several important advancements in the assessment of deep groundwater resources. It is the first to estimate permeability beyond depths of 1,000 m within a hard-rock environment and to develop detailed two and three dimensional permeability models through geophysical techniques. The innovative use of CSAMT for volumetric hydraulic parameter estimation represents a notable methodological breakthrough. Carried out in a geologically intricate setting dominated by sandstone, granite, and hornstone, where such deep assessments were previously unattempted, this work also highlights the effective integration of limited borehole data to generate high-resolution hydrogeological models. This strategy offers a practical and cost-efficient alternative to widespread deep drilling, significantly decreasing the number of boreholes required to achieve similar spatial detail in permeability mapping. The primary aim of this study is to develop and implement a geophysical-based approach for accurately predicting the spatial distribution of permeability in deep, hard rock environments. By integrating CSAMT data with strategically selected borehole measurements, this research enhances the two and three dimensional assessment of hydrogeological properties across various rock types in geologically complex settings, reduces reliance on extensive and costly drilling, and highlights the advantages of using non-invasive geophysical techniques as a more efficient alternative for deep groundwater exploration.

2 Methods

This study integrates limited drilling data with the CSAMT method to estimate permeability (k) for both two dimensional and three dimensional assessments of groundwater resources across the entire project area (Fig. 1a). The main stages of the methodology are summarized in the flowchart shown in Fig. 1b.

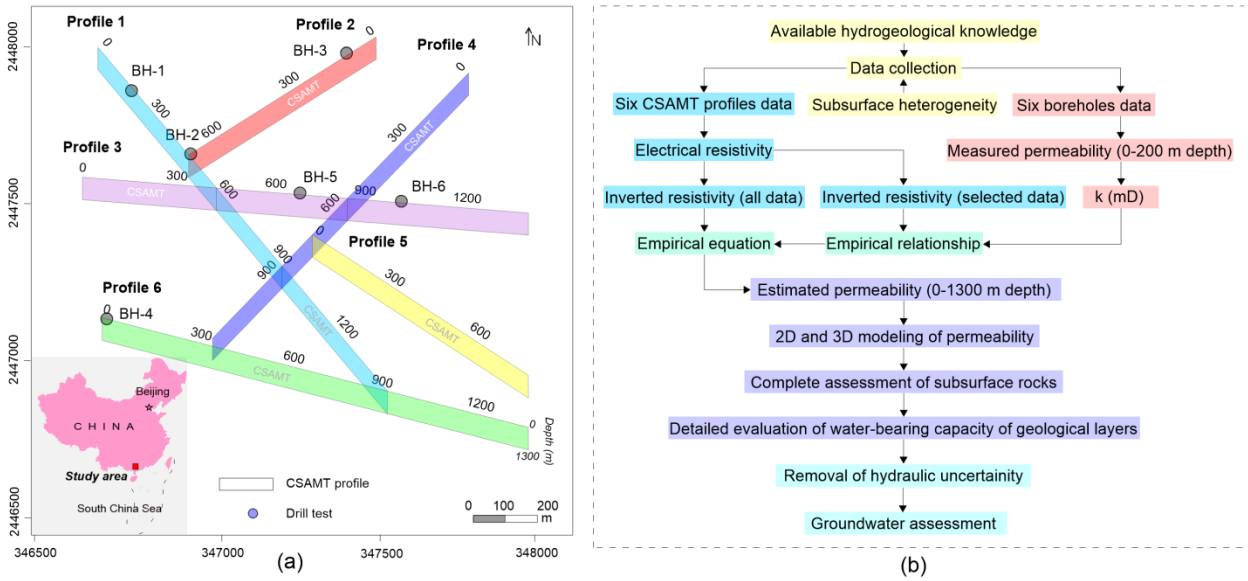

Fig. 1. (a) Location of the project site, showing six boreholes (BH-1 to BH-6) and six CSAMT survey profiles (1–6); (b) Flowchart illustrating the methodology for generating 2D and 3D permeability (k) models to enable comprehensive assessments of groundwater resources across extensive areas

2.1 Study area and hydrogeological settings

This study is part of a broader suite of major national-level initiatives in South Guangdong of China, each targeting distinct aspects of deep subsurface exploration. These include both the investigation of deep groundwater resources, as undertaken in this study, and the development of deep-underground engineering infrastructure, such as the Jiangmen Underground Neutrino Observatory (JUNO), China's next-generation neutrino detector (Hasan et al., 2025). While each project addresses distinct hydrogeological and geotechnical challenges, they are collectively aligned with China's broader strategic agenda for deep subsurface resource development and sustainable utilization. This study was conducted in the Jinji region of South Guangdong, a geologically diverse and structurally complex area prioritized for deep groundwater exploration (Fig. 1a). Situated within a subtropical monsoonal climate zone, the region experiences intense

seasonal rainfall, with an average annual precipitation of approximately 1981 mm. The topography is defined by low, eroded hills and moderately elevated mountains, with elevations ranging from 39 to 539.9 m above sea level. The study area features diverse topography, ranging from mild slopes to sharply inclined terrain, and is characterized by dense vegetation cover. The northern portion is comparatively flat, whereas the southern region is more mountainous, distinguished by notable elevations such as Dashishan, Qilongding, Jixinshan, and Xikeng. The Yongkouwei River, located in the northeastern section at approximately 7.5 m above sea level, is a crucial component of the region's surface water drainage system.

The Jinji region exhibits a complex geological evolution shaped by various tectono-magmatic events, particularly during the Caledonian (Silurian–Devonian), Indosinian (Late Triassic), and Yanshanian (Jurassic–Cretaceous) orogenic phases. The geodynamic episodes have resulted in a diverse lithological landscape, mainly consisting of granite, sandstone, and hornstone (hornfels) (Qin, 2017; Yang et al., 2021). Extensive granitic intrusions indicate deep crustal magmatism linked to continental collision and subduction processes. Hornstone exemplifies contact metamorphism resulting from the intersection of intrusive bodies with pre-existing sedimentary layers. Paleogene formations, primarily consisting of fluvial and lacustrine deposits, overlay these units and signify a subsequent phase of basin sedimentation. The region is characterized by the Kaiping concave fault-fold system, a significant deformation zone formed through recurrent crustal stress and magmatic processes. This structural framework encompasses various fault types, including reverse, thrust, and strike-slip, indicative of a prolonged history of crustal shortening and lateral displacement. Compressional folds that developed during the Caledonian and Indosinian periods were subsequently modified by strike-slip faulting in the Yanshanian phase. The prevalent northeast-trending orientation of these features aligns with

regional stress patterns and significantly influences the subsurface architecture (Qin, 2017; Yang et al., 2021). Fracture networks, consisting of joints and fissures, are widespread in granite, sandstone, and hornstone units. The brittle features, characterized by variations in spacing, orientation, and continuity based on lithology and structural history, function as essential conduits for groundwater flow. Their spatial alignment with major fault systems highlights a significant relationship between structural geology and hydrogeology, with critical implications for subsurface fluid dynamics in this fractured terrain.

This study primarily examines the vertical stratification of aquifer-bearing formations in the Jinji region. Highly productive groundwater zones are linked to deeply buried sandstone formations that possess well-developed fracture systems conducive to water storage and flow. The sandstone units are covered by a substantial granite layer with low permeability, which serves as a confining cap that limits vertical recharge from the surface. A hornstone (hornfels) stratum is situated between these two layers, exhibiting intermediate hydraulic properties while providing limited connectivity between the overlying granite and the deeper sandstone. This configuration effectively isolates deep sandstone aquifers from near-surface hydrological processes, making them inaccessible to conventional shallow geophysical or drilling techniques. Targeted deep exploration is essential for the accurate identification and characterization of concealed aquifers, as well as for guiding their sustainable management in this structurally complex hard rock environment.

2.2 CSAMT survey

2.2.1 Theoretical background

The application of CSAMT in hard rock studies is well documented, as evidenced by various publications (Simpson and Bahr, 2005; Bai et al., 2010; Fu et al., 2013; Wang et al., 2015; Wynn et al., 2016; Di et al., 2020; Zhang et al., 2021; Kouadio et al., 2023; Hasan et al., 2025). In such studies, a distant transmitter emits regulated electric signals into the earth, while a receiving station monitors the electric and magnetic fields (Zonge and Hughes, 1988; Zhang et al., 2021). A mathematical relationship exists between reflection depth and frequency in subsurface structures, where different fields exhibit varied propagation depths (Borah and Patro, 2019). This method utilizes the varying electrical conductivities of different rock types to monitor alterations in magnetic field strength and primary field potential (Cagniard, 1953; Zonge and Hughes, 1988). The frequency components of the signal are obtained from the time series of electromagnetic field fluctuations through the application of Fourier transforms (Simpson and Bahr, 2005). A regulated artificial field source is employed in CSAMT. Electrodes positioned one to two kilometers apart can measure the electromagnetic field component of an electric dipole source. The wires connecting the batteries to the current electrodes and the transmitter can be established. The typical distances between field source transmitters and receivers range from 5 to 10 km, although this may vary depending on the depth of investigation and geological conditions. A method for determining subsurface resistivity involves calculating the ratio of the magnitudes of the electric and magnetic fields measured in two orthogonal directions. Numerous studies, such as those by Fu et al. (2013), Zhang et al. (2021), and Hasan et al. (2024), have identified various factors affecting resistivity variations in connection with subsurface geological conditions. These factors include lithological variations in stratigraphic structures, fault-induced fragmentation, water saturation, rock types, pore fluid characteristics, and porosity. The vertical resolution in CSAMT, indicating the capacity to differentiate between neighboring subsurface

layers, generally varies from 5% to 20% of DOI (depth of investigation), which spans approximately 20 to 1000 meters. At shallower depths (e.g., 20–100 m), vertical resolution is higher (closer to 5%), enabling better differentiation between thin layers. At greater depths (up to 1000 m), resolution may degrade toward the 20% mark due to signal attenuation and broader averaging of resistivity data. This makes CSAMT a valuable tool for identifying significant lithological contrasts, fault zones, and resistivity anomalies related to geological structures. The propagation frequency and subsurface resistivity are the basis of DOI. According to Borah and Patro (2019), a lower frequency and higher resistivity typically result in a higher DOI. The distance between stations determines the lateral resolution; typically, this is between ten and two hundred meters. According to Simpson and Bahr (2005), increasing the distance between stations enhances the strength and reliability of the received signal. At every station, a portable receiver processes, amplifies, filters, and records the incoming signal. In order to pick up sent signals, electrode pairs, which include magnetic-field sensors and short grounded dipoles, are utilized. Effective survey planning plays a crucial role in minimizing the impact of metal fence, radio transmitter, power line, and other potential sources of interference that could affect the accuracy of CSAMT data. Plan, three-dimensional, fence, and cross-sectional views are all potential ways to display the modeled resistivity data.

2.2.2 Survey design and procedures

CSAMT data were collected along six profiles (Profiles 1–6), with a station spacing of 50 m between successive measurement points. The selection and location of 6 CSAMT profiles were chosen based on several factors, including geological targets and objectives, surface geology and mapping data, topography and terrain accessibility, orientation relative to structures, spacing and coverage requirements, resistivity contrast expectations, integration with other data (boreholes),

environmental and regulatory constraints, and source-receiver geometry requirements, etc. Carefully selected survey profiles enhanced the ability to resolve critical subsurface features and minimized ambiguities in the geophysical interpretation. The depth of investigation (DOI) in the CSAMT survey was about 1300 meters. We performed scalar measurements using the Transverse Magnetic (TM) mode, recording bidirectional magnetic and electric field components, both perpendicular and parallel to the survey line. For EMAP observations, measurement stations were arranged sequentially and placed approximately 50 m from the electrodes. The configuration utilized Gain Mode X1 along with a 50 Hz linear filter. Transmission current varied with frequency, ranging from 2.6–4.5 A at 7680 Hz to a peak of 12–18 A at 1 Hz. CSAMT data were collected using a V8 multifunction receiver coupled with a TXU-30 transmitter, both produced by Phoenix Geophysics, Canada. The TXU-30 is a versatile, high-power transmitter with a maximum output capacity of 30 kilowatts. It enables geophysical operation with transmission voltages up to 1000 V, delivering currents up to 20 A at 1000 V and up to 40 A at 500 V. This GPS-enabled transmitter is ideal for deep investigation since it is compatible with common household three-phase 220 volt alternators. There were 34 separate frequency points utilized, spanning the range of 1–7680 Hz. In addition to collecting data, the V8 multifunction receiver may monitor data sent by other secondary receiving units. The principal receiver's three channels and tracks make this possible. The distances between the transmitter and receiver stations ranged from 9.3 to 12.5 km. Non-polarized electrodes were used to record the electric field signals. Magnetic signals were captured using the AMTC-30 inductive sensor, specifically designed for high-frequency AMT/CSAMT applications, with an operational range from 10,000 Hz to 0.1 Hz. At each site, two orthogonal components of the electric field and three orthogonal components of the magnetic field were acquired, allowing for the computation of the

full impedance tensor. Positional data for all measurements were obtained using a Trimble XH dual-frequency GPS receiver, manufactured in the United States. Using the Hi-Tech V30GNSS RTK apparatus, we measured the CSAMT lines for object recognition. Modern navigational aids allow for pinpoint accuracy on the order of sub-meter precision. The computer calculated the coordinate values of each survey line and survey point using the given direction and distance, and then sent them to the GPS or RTK. Survey line measurement points were identified using RTK or GPS navigation systems. The spatial distribution of inspection points was consistently maintained, with system quality assessments showing variability within a 3–5% range along the measurement lines. The system quality assessment met the following design criteria: a root-mean-square (RMS) error of less than ±5%, an allowable error of less than 10 between consecutive profile points, a relative elevation tolerance of 1.67 mm, and a planar tolerance of 2.33 mm. Due to the absence of anthropogenic and electrical interference at the survey site, the collected data was of exceptionally high quality. Site characteristics were interpreted based on the analysis of the CSAMT data (An and Di, 2016; Hasan et al., 2025). After eliminating skewed data, a detailed curve analysis was performed..

2.2.3 Processing workflow

Static correction and spatial filtering using a Hanning window are essential preprocessing steps in CSAMT data analysis, aimed at improving data quality and enhancing the reliability of subsurface resistivity models. Static correction mitigates the impact of near-surface resistivity inhomogeneities, which can distort electric field measurements and result in static shifts, leading to vertical displacements in apparent resistivity curves that misrepresent deeper subsurface conditions. To improve data quality, measured electric fields were calibrated against a stable baseline or averaged field, thereby reducing the impact of shallow subsurface layers and isolating

signals from deeper sources. Simultaneously, spatial filtering techniques were employed to mitigate noise resulting from environmental and instrumental interference. The Hanning (Hann) window demonstrated notable effectiveness in suppressing spectral leakage and smoothing fluctuations while preserving underlying trends. The Hanning window, when applied in spatial filtering, executed weighted averaging among adjacent measurement stations, preserving coherent spatial patterns and reducing high-frequency noise. This method markedly enhanced the stability and interpretability of the resulting inversion models. For the data processing step, we used the CMTPro Version software produced by Phoenix Geophysics (Phoenix Geophysics CMTPro, 2020). This program combines V8 and tracking data, and source current into CMT files, corrects electrode coordinates, automatically smoothes observed curves, and generates files in the AVG format, among other things. Fig. 2 shows a flow diagram of the CSAMT-SW method (Phoenix Geophysics CSAMT-SW, 2020) that was used to conduct the 2D inversion (Rodi and Mackie, 2001; Wang et al., 2015).

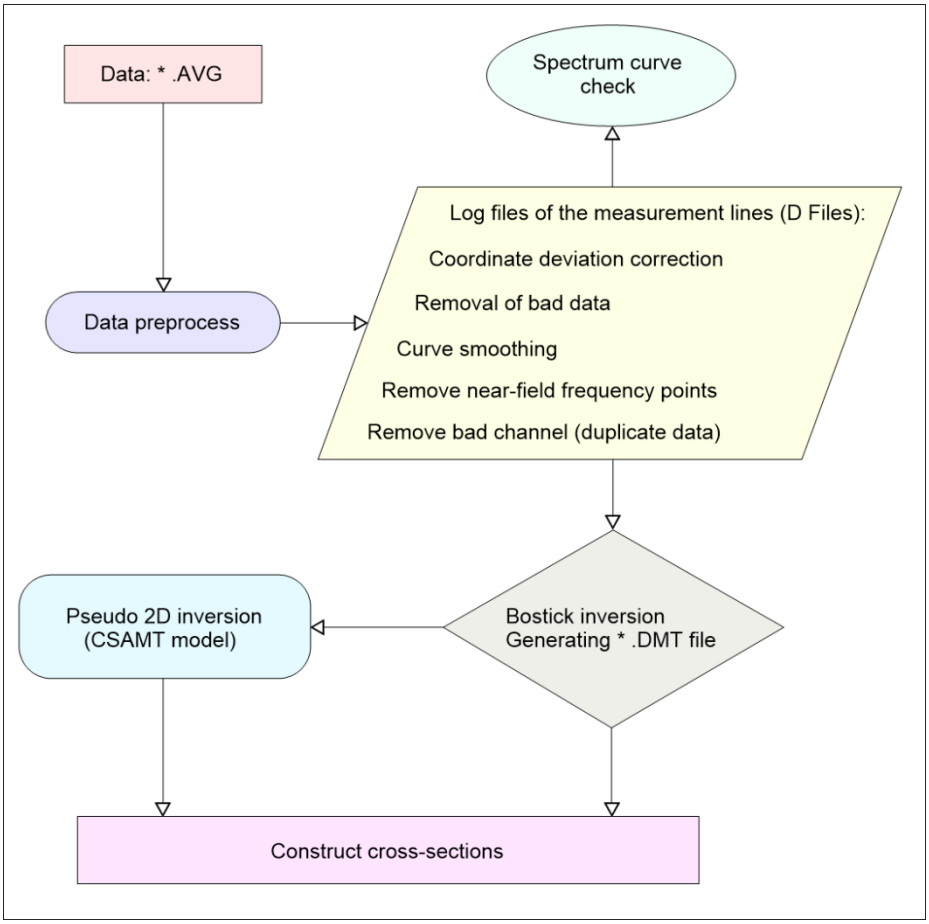

Fig. 2. Illustration of the 2D inversion process of CSAMT data using Bostick inversion

Here are the main components of the CSAMT-SW: 1. Data format conversion from AVG to D; 2. Editing and generating CHK elevation files, and converting them to format D; 3. Manually checking the file D for corrupted sectors, filling in the gaps, removing near-field data, and skipping to certain spots; 4. Inversion outcomes from different static correction methods were very similar when compared; the D file was utilized for smoothing processing; 5. D, H, K, and Z are the four static correction results files for various correction approaches; 6. Generating text files through BOSTICK inversion combined with near-field correction; 7. Using quasi-2D inversion combined with the CSAMT global field model (ID), which integrates both near and transition fields, finite-depth layers representing resistivity variations can be generated directly

from the measured CSAMT data. After applying Bostick inversion (Fusheng et al., 2022), the output data in D format were saved as *_BOS.DAT and *_BSS.DAT files, respectively. The processed data, formatted according to the requirements of the CSAMT 2D inversion model, were stored in a newly created *_M.DMT text file. The inversion process continued until either the maximum number of iterations, set at five, or the target RMS error was reached. At this point, the resulting models were fitted to the observed data using the inversion method. A trustworthy 2D resistivity model (Zhang et al., 2021) of CSAMT was produced, considering the local geology and dataset quirks, by employing the most appropriate processing and inversion procedures to reduce model errors. The final inversion models (Fig. 3), through delineation of resistivity variations, significantly enhanced our understanding of the subsurface geological framework.

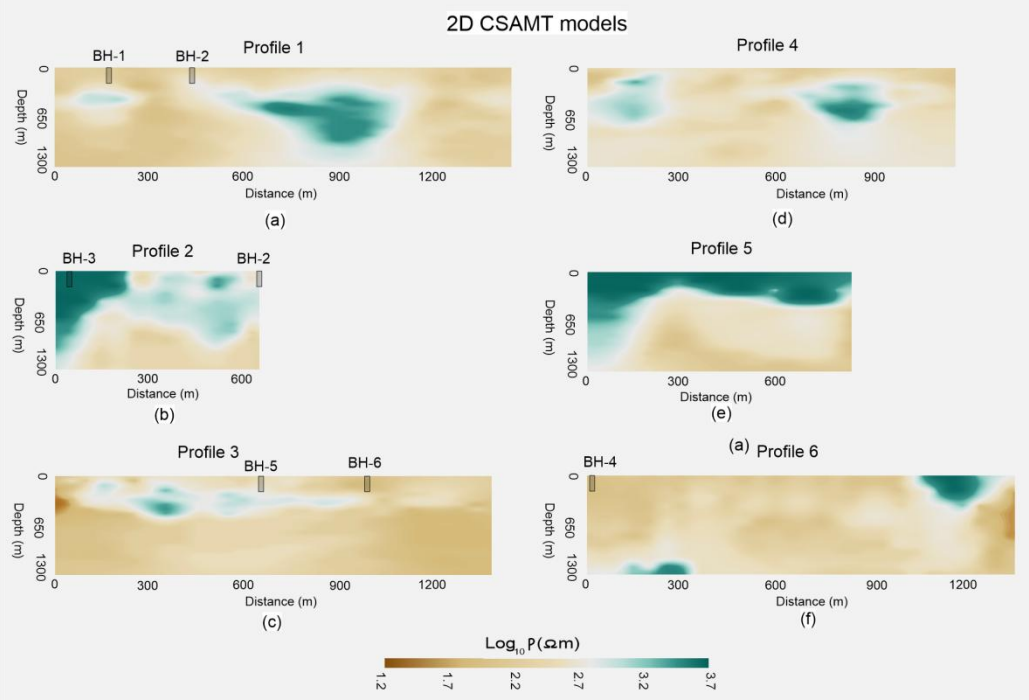

Most of figures not clear , some questions
1-Why the length of profiles do not have the same?
2-The scale of resistivity not clear can you put it in linear scale?
3-The depth of boreholes is very shallow with respect to MT sections for correlation

Fig. 3. Construction of 2D CSAMT models along six geophysical profiles: (a) Profile 1, (b) Profile 2, (c) Profile 3, (d) Profile 4, (e) Profile 5, and (f) Profile 6. Resistivity values increase from brown to green on the color scale.

2.3 Permeability estimation framework

2.3.1 Laboratory-based permeability determination from borehole core samples

Permeability (k) is a fundamental hydrogeological parameter that describes the capacity of a porous medium, such as rock or sediment, to transmit water. This concept is crucial for comprehending fluid dynamics in aquifers and is extensively utilized in groundwater evaluations (Allègre et al., 2016; Fiandaca et al., 2018; Mudunuru et al., 2022; Esmaeilpour et al., 2023; Carbillet et al., 2024). The permeability of a formation indicates the extent to which fluids can move through pore spaces or interconnected fractures, serving as a critical factor in subsurface hydrodynamics at different depths. k is typically determined via pumping tests or direct testing of rock cores collected from boreholes, a method that is both expensive and logistically demanding. Permeability is affected by various geological and physical factors, including porosity, lithological composition, saturation level, faulting, jointing, and diagenetic processes such as compaction and mineral alteration (Dewandel et al., 2006; Yan et al., 2024).

In this study, the initial permeability data from the Jinji region were limited to just six boreholes. A suite of laboratory analyses was conducted on rock core samples obtained from the deep boreholes to enhance the dataset's robustness. The research concentrated on three primary lithologies: sandstone, hornstone (hornfels), and granite. The samples covered depths reaching 200 m. A total of 116 laboratory measurements were collected, comprising 31 from sandstone, 23 from hornstone, and 62 from granite. These measurements offer significant insights into the

vertical distribution of permeability across various strata, thereby enhancing the hydrogeological characterization of the region (Neuzil, 1994; Zhang et al., 2020).

Coring was performed utilizing a wireline rotary system equipped with triple-tube barrels to achieve minimal disturbance and optimal recovery of intact samples (ISRM, 2007). Core samples were promptly vacuum-sealed and stored under controlled humidity to maintain in-situ moisture conditions and the integrity of microfracture networks. Before testing, cores were sectioned into standardized cylindrical specimens, generally measuring 50 mm in diameter and 100 mm in length, and examined to eliminate any visibly fractured or altered areas.

Two distinct laboratory techniques were utilized according to the anticipated permeability range of each rock type. A steady-state flow method was employed for sandstone, which typically demonstrates higher permeability, in accordance with ASTM D5084-21 guidelines (ASTM, 2021). A constant hydraulic gradient was applied under fully saturated conditions, and the corresponding volumetric flow rate was recorded. Permeability was determined through the application of Darcy's Law:

$$k = \frac{Q \cdot \mu \cdot L}{A \cdot \Delta P} \quad (1)$$

where Q is the flow rate (m^3/s), μ is the fluid viscosity (Pa·s), L is the sample length (m), A is the cross-sectional area (m^2), and ΔP is the applied pressure difference (Pa).

The transient pulse decay method was employed for granite and hornstone, both of which exhibit low permeability, adhering to the procedure originally outlined by Brace et al. (1968) and subsequently refined by Hsieh et al. (1981). This method involves introducing a brief pressure pulse at one end of the saturated specimen and monitoring the rate of pressure decay over time. Tests were performed under confining pressures reaching 30 MPa to replicate in-situ stress

conditions and to examine the stress-sensitive behavior of crystalline rocks, where fracture closure can notably influence permeability (Faybishenko et al., 2000; Niu et al., 2016).

Each lithology underwent testing under both dry and saturated conditions to assess the influence of moisture content on permeability. Measurements were replicated to ensure data reliability, and statistical analyses were employed to evaluate variability within and among lithological groups (Zhao et al., 2018). The permeability data were organized by depth and lithology to create vertical permeability profiles, which served as a crucial input for analyzing the hydrostratigraphic framework of the subsurface. Granite demonstrated the lowest permeability, indicative of its dense, unfractured crystalline structure. Hornstone exhibited intermediate permeability values, probably resulting from localized tectonic or thermally induced fractures. Conversely, sandstone layers at increased depths exhibited markedly higher permeability, aligning with their function as the primary aquifer units in the study region (Wang et al., 2014; Liu et al., 2021).

2.3.2 Permeability-resistivity relationship (Archie and Kozeny-Carman equation)

Several foundational studies have established empirical and theoretical relationships between electrical resistivity and hydraulic properties such as permeability. The Archie equation, introduced by Archie (1942), is widely used in clean, saturated sedimentary formations. It relates formation resistivity to porosity and water saturation but assumes the absence of clay minerals and thus has limitations in more complex lithologies (Waxman & Smits, 1968; Glover, 2015). The Kozeny-Carman equation is another widely accepted model that links permeability to porosity and specific surface area (Bear, 1972; Carman, 1956). While it does not directly involve resistivity, it is often used alongside petrophysical models to interpret hydrogeological characteristics based on geophysical data (Paterson & Wong, 2005; Clennell, 1997).

Archie's law (Archie, 1942) relates the bulk electrical resistivity of a fully saturated porous medium to its porosity and fluid resistivity. It is commonly expressed as:

$$\rho b = a \cdot \rho f \cdot \phi^{-m} \quad (2)$$

where, ρb is the bulk resistivity, ρf is the fluid resistivity, ϕ is the porosity, a and m are empirical constants. Although Archie's law does not directly estimate permeability, porosity is often used as a proxy because of its influence on fluid flow. The resistivity-porosity relationship can be indirectly extended to infer permeability, especially when combined with other petrophysical models (Binley et al., 2005; Revil & Cathles, 1999).

The Kozeny–Carman equation establishes a theoretical relationship between permeability (k) and porosity (ϕ), expressed as follows:

$$k = \frac{C \cdot \phi^3}{(1-\phi)^2 . S^2} \quad (3)$$

In this equation, k denotes permeability, ϕ represents porosity, S is the specific surface area, and C is a structural constant reflecting pore geometry and tortuosity. The application of this equation alongside Archie's law facilitates the development of empirical or semi-empirical models that connect electrical resistivity to permeability (Jiang et al., 2014; Jardani et al., 2007).

Although these formulations offer a robust theoretical foundation, their direct application in complex geological contexts, particularly in heterogeneous hard rock such as granite, sandstone, and hornstone, is frequently limited. This results mainly from differences in mineral composition, pore connectivity, and structural anisotropy (Roa-García et al., 2010; Singh et al., 2020). Our present study establishes a localized empirical relationship between resistivity and permeability through co-located measurements obtained from deep boreholes and CSAMT profiles to address these challenges. Such correlation facilitates the development of high-

503 resolution 2D and 3D permeability models in the Jinji area (study area), thereby improving the
504 comprehension of subsurface hydrogeology in contexts where traditional methods fall short.

505 **2.3.3 Spatial permeability modeling from CSAMT data**

506 To estimate permeability (k) across the entire study area, we implemented a multi-stage
507 approach integrating borehole core analysis with CSAMT-derived resistivity data. In the first
508 stage, a total of 116 laboratory-based permeability measurements were acquired from six
509 boreholes (from BH-1 to BH-6), drilled to depths ranging from 0 to 200 m (Fig. 4). These
510 measurements were obtained from intact rock core samples representing three principal
511 lithologies: granite, hornstone, and sandstone.

512 In the second stage, each of the 116 borehole-derived k values was empirically correlated
513 with corresponding resistivity values extracted from CSAMT soundings co-located with the
514 borehole sites. The spatial correspondence between boreholes and CSAMT sounding points was
515 carefully matched (Fig. 4). For example: P1-5 represents the fifth CSAMT sounding at 200 m
516 along survey line 1 near borehole BH-1; P1-9 corresponds to the ninth sounding at 400 m on line
517 1 near borehole BH-2; P2-3 denotes the third sounding at 100 m along line 2 near BH-3; P6-1
518 indicates the first sounding at 0 m on line 6 adjacent to BH-4; P3-15 and P3-21 represent the
519 fifteenth (700 m) and twenty-first (1000 m) soundings along line 3, near boreholes BH-5 and
520 BH-6, respectively.

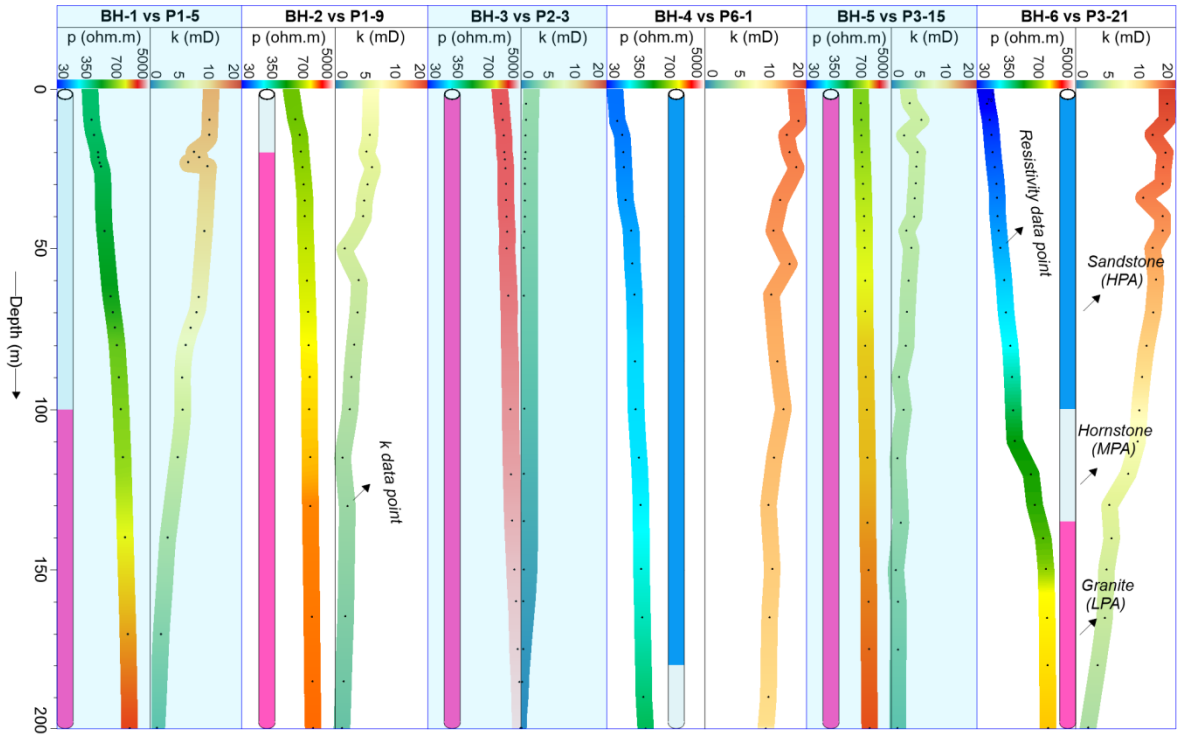

Fig. 4. Comparison of 116 CSAMT-based resistivity (ρ) data points with corresponding drilling-based permeability (k) values at depths of 0–200 m across six borehole locations (BH-1 to BH-6). The data were used to evaluate high potential aquifers (HPA) in sandstone, medium potential aquifers (MPA) in hornstone, and low potential aquifers (LPA) in granite. Each dot represents a resistivity or permeability data point. Sounding labels indicate specific CSAMT locations: P1-5 (5th point on Line 1), P1-9 (9th on Line 1), P2-3 (3rd on Line 2), P6-1 (1st on Line 6), and P3-15 and P3-21 (15th and 21st on Line 3.)

In the third stage, all 116 paired measurements of permeability (k) and resistivity (ρ) were utilized to develop an empirical model. An exponential relationship was derived between permeability (k in millidarcies or mD) and electrical resistivity (ρ in Ωm), expressed as follows (Fig. 5):

$$k = 15.373(e)^{-0.002(\rho)} \quad (4)$$

This site-specific empirical model was then applied to the entire suite of CSAMT resistivity data collected along six survey profiles to estimate spatial variations in permeability across the broader study area. Using this relationship, we generated predictive 2D and 3D permeability models that capture the hydraulic behavior of three major lithological units: low potential aquifer (LPA): associated with low-permeability granite, medium potential aquifer (MPA): hosted within fractured hornstone (hornfels), high potential aquifer (HPA): corresponding to more porous sandstone units.

These models provide a depth-resolved assessment of subsurface permeability from the surface down to approximately 1300 m. Final 2D and 3D spatial visualizations were developed using Geosoft Oasis montaj and SKUA-GOCAD modeling platforms (Webring, 1981; Mira Geoscience Ltd., 1999; Hasan et al., 2024), enabling the visualization of permeability distributions across all six CSAMT profiles and improving hydrogeological characterization in structurally complex hard rock terrain.

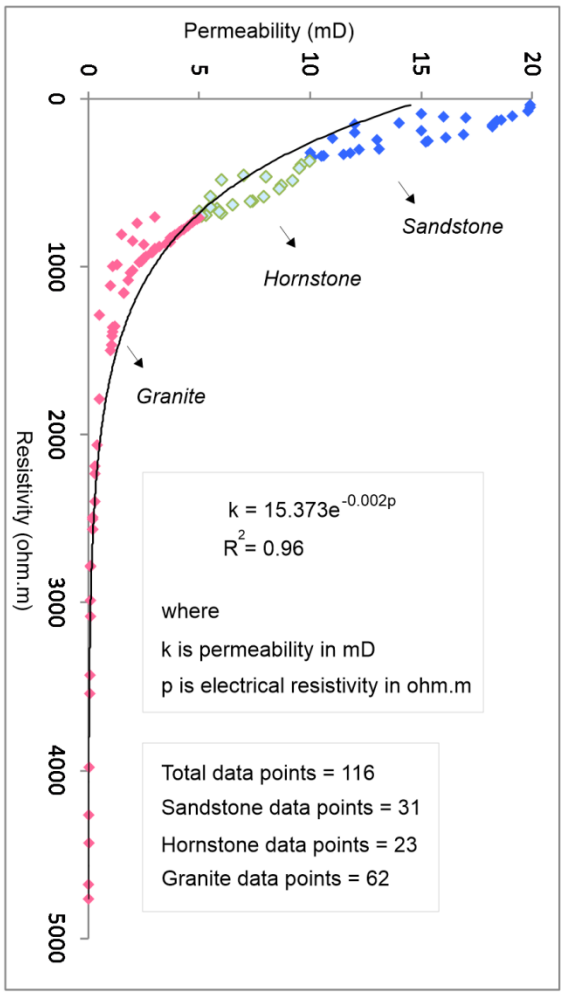

Fig. 5. Empirical relationship derived from 116 data points comparing CSAMT-based resistivity and drilling-based permeability at depths of 0–200 m, across three lithologies: sandstone (31 data points), hornstone (23 data points), and granite (62 data points).

3 Results

3.1 Cross-validation of geophysical and borehole parameters

Table 1 summarizes the integrated dataset from six boreholes and six CSAMT profiles, which were used to delineate the subsurface into three distinct hydrogeological units, based on variations in electrical resistivity and corresponding permeability (k) values. The development of

these subsurface models mainly depends on borehole data, CSAMT-derived resistivity measurements, and the regional geological framework. The stratigraphy was categorized into three primary lithologies: sandstone, hornstone, and granite. Classification criteria were established as follows: sandstone was defined by resistivity values below 350 Ωm and a permeability range of 10–20 mD; hornstone exhibited resistivity values between 350 and 700 Ωm with a k range of 5–10 mD; and granite was characterized by resistivity values exceeding 700 Ωm and permeability values ranging from 0 to 5 mD. Based on our evaluations of the subsurface hydrogeological model's aquifer potential zones, we found that sandstone contains the high potential aquifer (HPA), hornstone contains medium potential aquifer (MPA), and granite has low potential aquifer (LPA). Aquifers with the largest yields or the best water-bearing capacity are indicated by sandstone, whereas aquifers with the lowest yields or the worst water-bearing capacities are denoted by granite. Groundwater development is best facilitated by sandstone in the study area, whereas groundwater extraction is most hindered by granite.

Table 1

Integrating distinct ranges of electrical resistivity and permeability (k) enables a comprehensive assessment of groundwater potential across various hard rock types

Resistivity (Ωm)	k (mD)	Type of rock	Aquifer potential
< 350	10–20	Sandstone	High potential aquifer (HPA)
350–700	5–10	Hornstone	Medium potential aquifer (MPA)
>700	0–5	Granite	Low potential aquifer (LPA)

3.2 2D groundwater assessments

572 Using geophysical-borehole correlation as its basis, Eq. (4) efficiently converts two dimensional
573 CSAMT models (Fig. 3) into two dimensional k models (Fig. 6). The interpreted 2D k models
574 shown in Fig. 7, in comparison with the limited borehole experiments, allow for an accurate and
575 comprehensive assessment of the groundwater resources in hard rock across the whole research
576 area, from 0 to 1300 m deep.

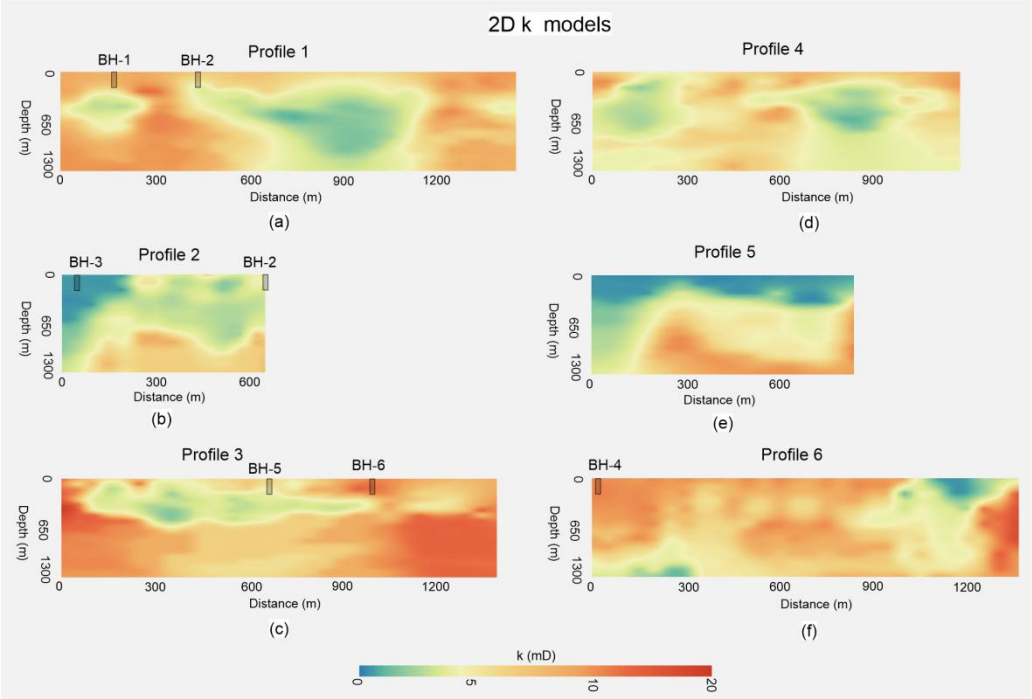

577

578 **Fig. 6.** The predicted 2D k models along six geophysical profiles: (a) Profile 1, (b) Profile 2, (c) Profile 3,
579 (d) Profile 4, (e) Profile 5, and (f) Profile 6. k values increase from blue to red on the color scale.

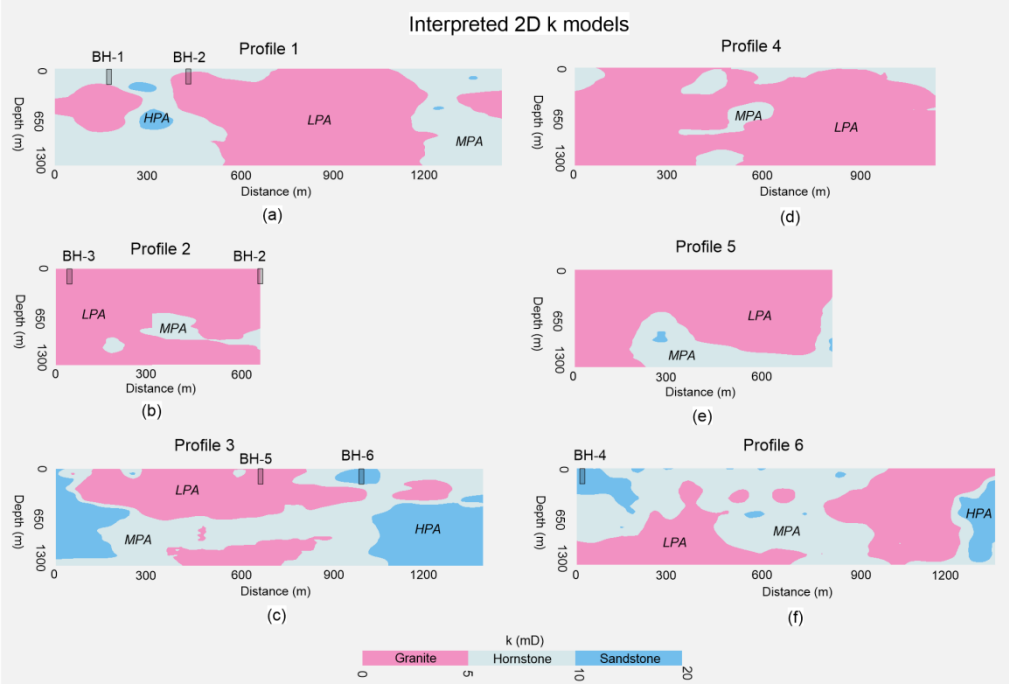

580

581 **Fig. 7.** The interpretation of the predicted 2D k models along six geophysical profiles: (a) Profile 1, (b)
582 Profile 2, (c) Profile 3, (d) Profile 4, (e) Profile 5, and (f) Profile 6. Sandstone is represented in blue,
583 hornstone in light blue, and granite in pink

584 The integrated 2D k models (Fig. 8) and their interpretation (Fig. 9) offers a more
585 comprehensive and detailed two dimensional evaluations of groundwater resources within the
586 highly heterogeneous geological settings of sandstone, hornstone, and granite. Line 1 of the
587 survey has had the following geological layers marked out for the purpose of groundwater
588 evaluation: A sandstone layer of high potential aquifer, 85 to 305 m thick, is visible between 245
589 and 380 m of distance, at depths ranging from 205 to 400 m. From 0 to 1300 m below surface, at
590 concentrations of 0 to 525 m and 1185 to 1445 m away, the remaining portion of the profile is
591 composed of a medium potential aquifer embedded in sandstone. Distances of 0–285 m within
592 290–790 m depth, 385–1185 m between 0–1300 m depth, and 1305–1450 m within 390–745 m
593 depth were used to assess granite aquifers with poor potential. Along profile 2, the geological

layers that were employed for groundwater assessment are described as follows: A hornstone layer 140–380 m thick encloses a medium potential aquifer 490–1105 m below ground, more precisely between 145–215 m and 290–645 m distance. We did not detect any sandstone associated with the high potential aquifer along this profile. Along this profile, granite from low potential aquifers predominates, with the exception of the zones evaluated by medium potential hornstone aquifers; granite is located at 0–700 m distance between 0–1300 m depths. Along profile 3, the following geological layers have been characterized for the purpose of groundwater evaluation: A hornstone-containing medium potential aquifer is evaluated at depths between 0 and 1300 m and within a range of 0 to 1400 m distance. Sandstone-associated high potential aquifers are located between 0 and 250 m distance and between 0 and 1190 m depths; 905 and 1065 m away between 0 and 205 m deep; and 1040 and 1390 m distance and between 490 and 1305 m depths. Distances of 80–1015 m between 0–590 m depths, 395–845 m between 915–1300 m depth, and 1100–1300 m between 200–500 m depth are used to assess the possible aquifers contained beneath granite. Here is the breakdown of the geological layers in profile 4 for the purpose of groundwater assessment: The hornstone medium potential aquifer is checked at distances of 0–105 m and depths of 0–340 m. There is a layer about 290 m thick hornstone at 0–1300 m depth between 340 and 645 m distances, with depths of 0–300 m between 595 and 790 m profile spread, and 0–345 m deep between 1015 and 1145 m distance. No sandstone that could contain a high potential aquifer is being investigated along this profile. The low potential aquifer associated with granite is delineated at most portions of the profile at 0–1145 m distance between 0–1300 m depths, excluding the areas with medium potential aquifer of hornstone. The geological layers that were considered for the groundwater assessment along profile 5 are as follows: Between 190 and 845 m beneath the granite, there is hornstone associated with a

617 medium potential aquifer, which is located between 390 and 1325 m below the surface. Two
618 small sandstone patches of high yield aquifer can also be seen along this profile. One is at 790–
619 960 m depth for 290 m distances, while the other is at 815 m, between 1045 and 1135 m depth.
620 Within the depth range of 0–1300 m, granite from low potential aquifers is assessed at a distance
621 of 0–190 m, and between 0 and 1025 m, at a distance of 790–815 m. Here are the geological
622 layers that can be used for groundwater assessment along profile 6: To assess the high potential
623 aquifer linked to sandstone, distances of 0–190 m between depths of 0–490 m and 1245–1345 m
624 between depths of 215–1225 m are utilized. Distances of 0–690 m within depths of 390–1300 m
625 and 790–1360 m within 0–1190 m depths are used to evaluate low yield aquifer granite. Between
626 0 and 1300 m depth and 0 and 1350 m distance, the hornstone of the medium potential aquifer
627 dominates the rest of the profile. In the southeastern and northwest regions, there are a lot of
628 medium to high potential aquifers, according to the results of the integrated 2D k models shown
629 in Fig. 8 and 9. On the other hand, in the central areas, groundwater resources are scarce or
630 nonexistent.

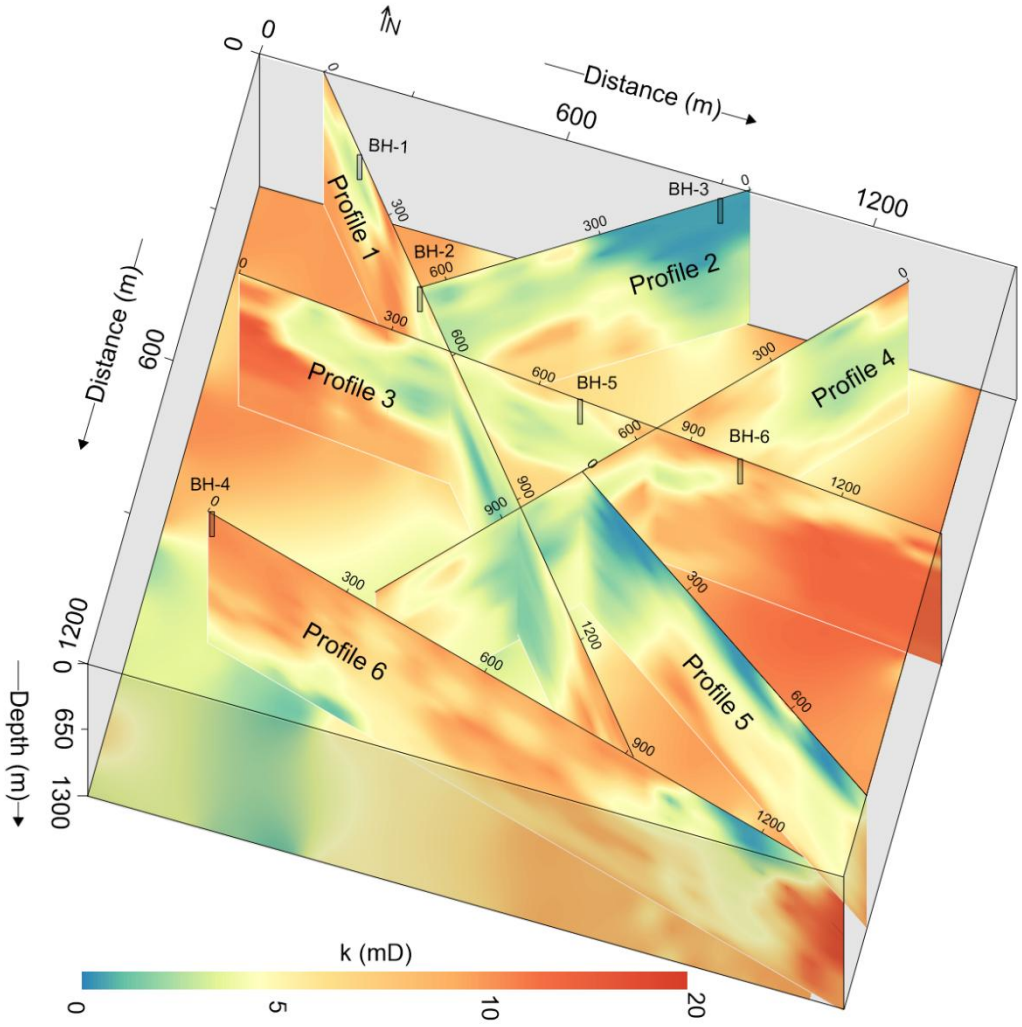

631

632 **Fig. 8.** The integrated 2D k models derived from the incorporation of geophysical and drilling data, with k

633 represented on a color bar spanning from green to red

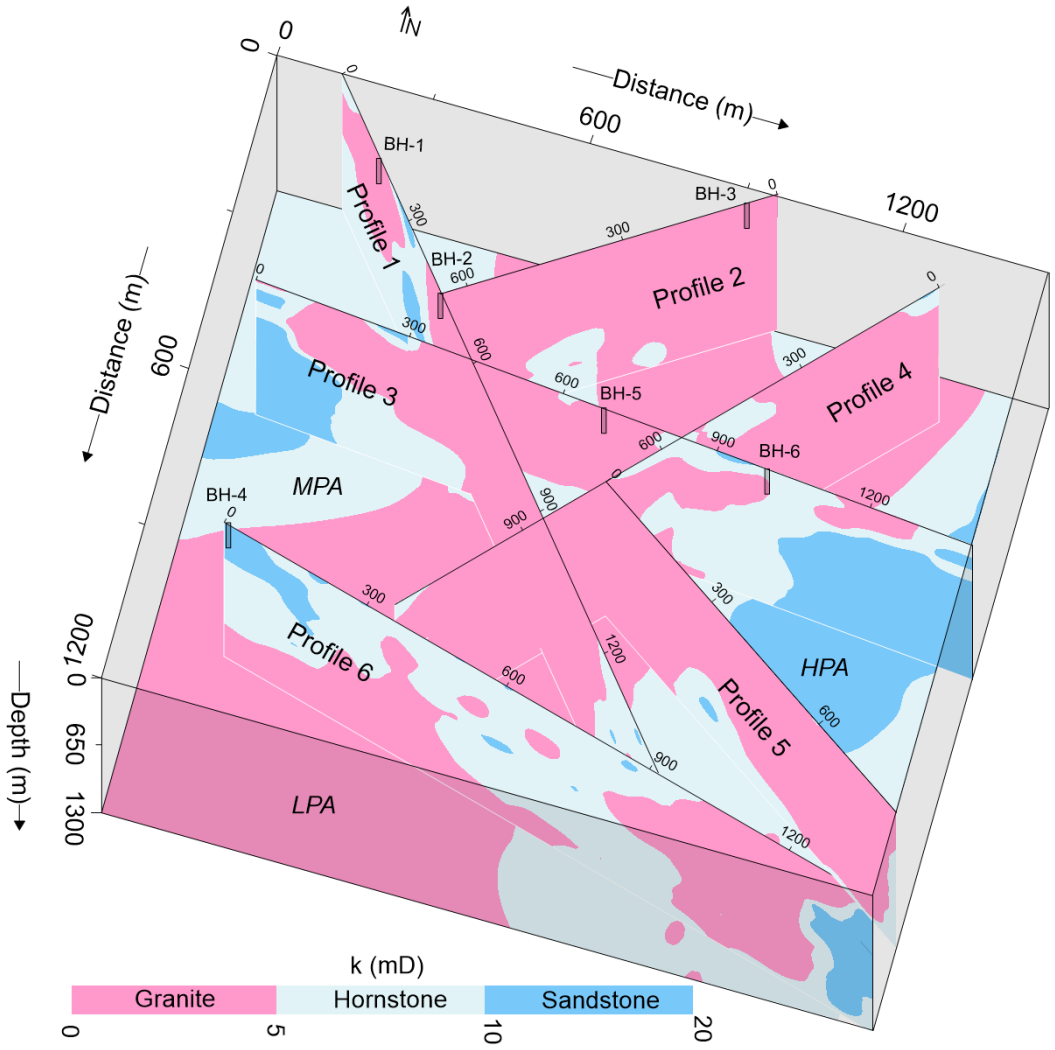

634

635 **Fig. 9** Analysis of 2D permeability (k) models, based on defined k ranges, for three groundwater potential
636 aquifers: low potential aquifer (LPA), medium potential aquifer (MPA), and high potential aquifer (HPA),
637 corresponding to the granite, hornstone, and sandstone formations, respectively

638 **3.3 3D groundwater assessments**

639 A thorough assessment of the water-bearing capacity of the rock mass for groundwater
640 evaluation was conducted using the 3D k external visualization depicted in Fig. 10 (a, b). The
641 granite of low potential aquifer was evaluated at the ground surface along profile 1 at distances
642 of 85–215 m and 385–1175 m, surveyed line 2 at 0–655 m, CSAMT line 3 at 0–45 m, 95–175 m,

643 265–585 m, 605–845 m, and 1145–1315 m, line 4 at 90–390 m, 490–615 m, and 745–1115 m,
644 line 5 at 0–815 m, and surveyed line 6 at 1045–1345 m. A medium potential aquifer within
645 hornstone was identified along profile 1 at distances of 0–95 m, 190–260 m, 295–415 m, and
646 1185–1425 m; along profile 3 at 40–105 m, 215–275 m, 580–605 m, 850–910 m, 1010–1155 m,
647 and 1310–1410 m; along profile 4 at 45–90 m, 390–490 m, 590–685 m, and 1115–1185 m; and
648 along line 6 at 90–190 m, 215–275 m, 315–485 m, 505–605 m, and 635–1045 m. The sandstone
649 with significant aquifer potential was assessed across many locations: profile 1 at distances of
650 265–310 m, line 3 at 235–255 m and 915–1010 m, profile 4 within 0–45 m, and profile 6 at 0–90
651 m, 210–25 m, 275–305 m, 515–525 m, and 605–635 m. Fig. 10 indicates that elevated aquifer
652 yield is predominantly concentrated in the southern regions.

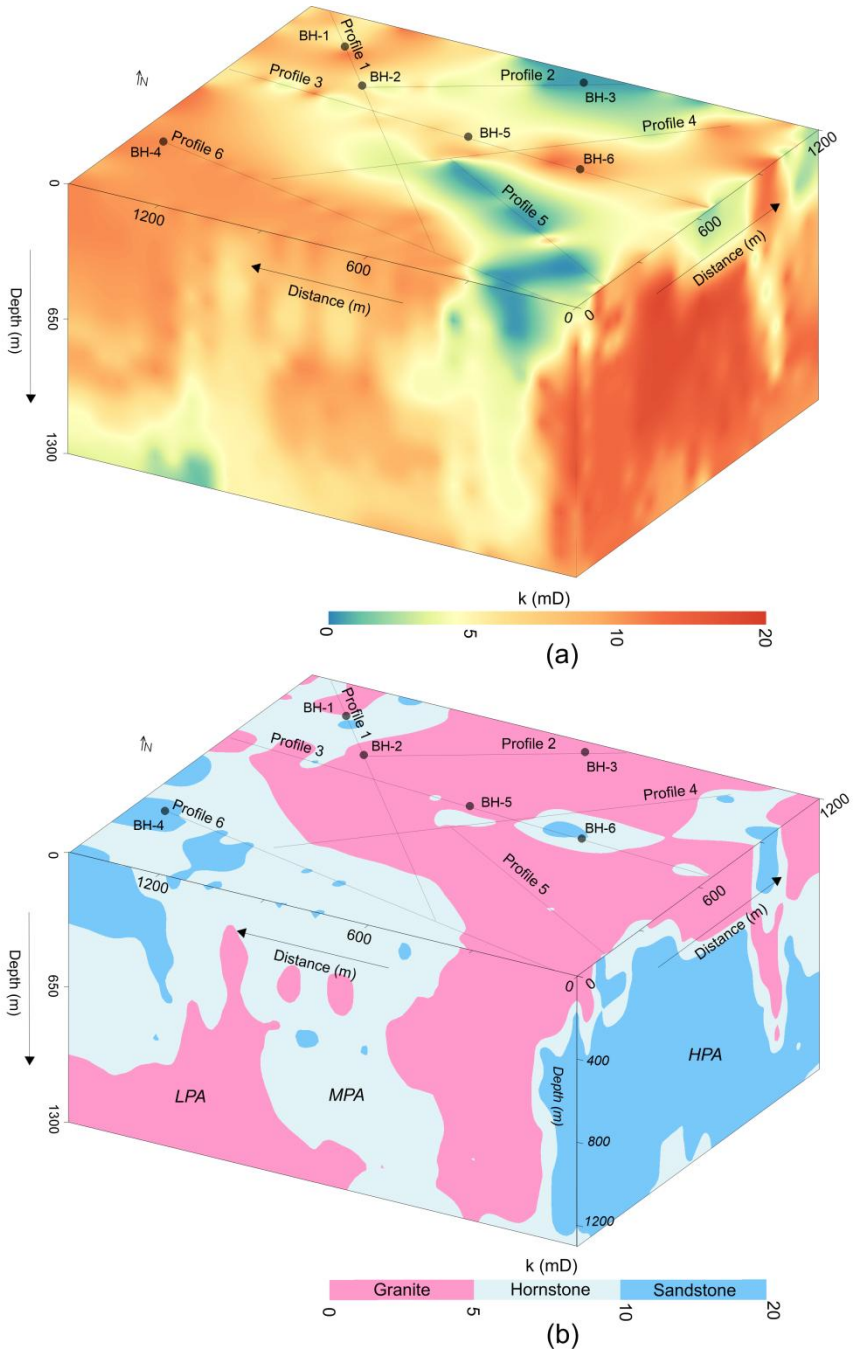

653

654 **Fig. 10.** The 3D k models, generated from the correlation of CSAMT and borehole data (with k
655 represented on a color scale ranging from green to red), correspond to three groundwater potential
656 aquifers: low potential aquifer (LPA), medium potential aquifer (MPA), and high potential aquifer (HPA),
657 associated with three geological strata: granite, hornstone, and sandstone, respectively, for (a) the external
658 view of the 3D k model, and (b) the analysis of the 3D k model from an external perspective

Fig. 11 (a, b) presents a comprehensive evaluation of the aquifer potential of the rock mass for groundwater assessment, using a 3D internal perspective. At a subterranean depth of 1300 m, the low aquifer yield of granite was assessed using profile 1 across a distance of 515–1215 m, profile 2 across 0–290 m, profile 3 across 390–690 m, profile 4 across 0–1145 m, profile 5 across 0–195 m and 565–595 m, and profile 6 across lengths of 0–690 m and 1075–1115 m. Hornstone associated to a medium potential aquifer was identified by profile 1 at intervals of 0–540 m and 1215–1445 m, surveyed line 2 at 295–675 m, surveyed line 3 at 175–395 m, 445–815 m, and 915–1035 m, profile 5 at 205–565 m and 610–815 m, and surveyed line 6 at 685–1080 m and 1110–1355 m. An aquifer with high potential, situated within sandstone, was evaluated along profile 3 at intervals of 0–205 m and 1010–1400 m, as well as along line 5 at 810–815 m. Medium to high potential aquifers, located at a depth of 1300 m, are predominantly found in the southeastern and northwestern regions, whilst the central areas are primarily characterized by low potential aquifers. Fig. 11 illustrates the results of the 3D K analysis, indicating that the northeastern and southwestern regions are primarily composed of granite with negligible aquifer yield. The water retention capacity of the rock mass is enhanced when observed from an aerial perspective. This enables a precise assessment of the aquifer potential of geological strata for thorough groundwater analysis via 3D k modeling.

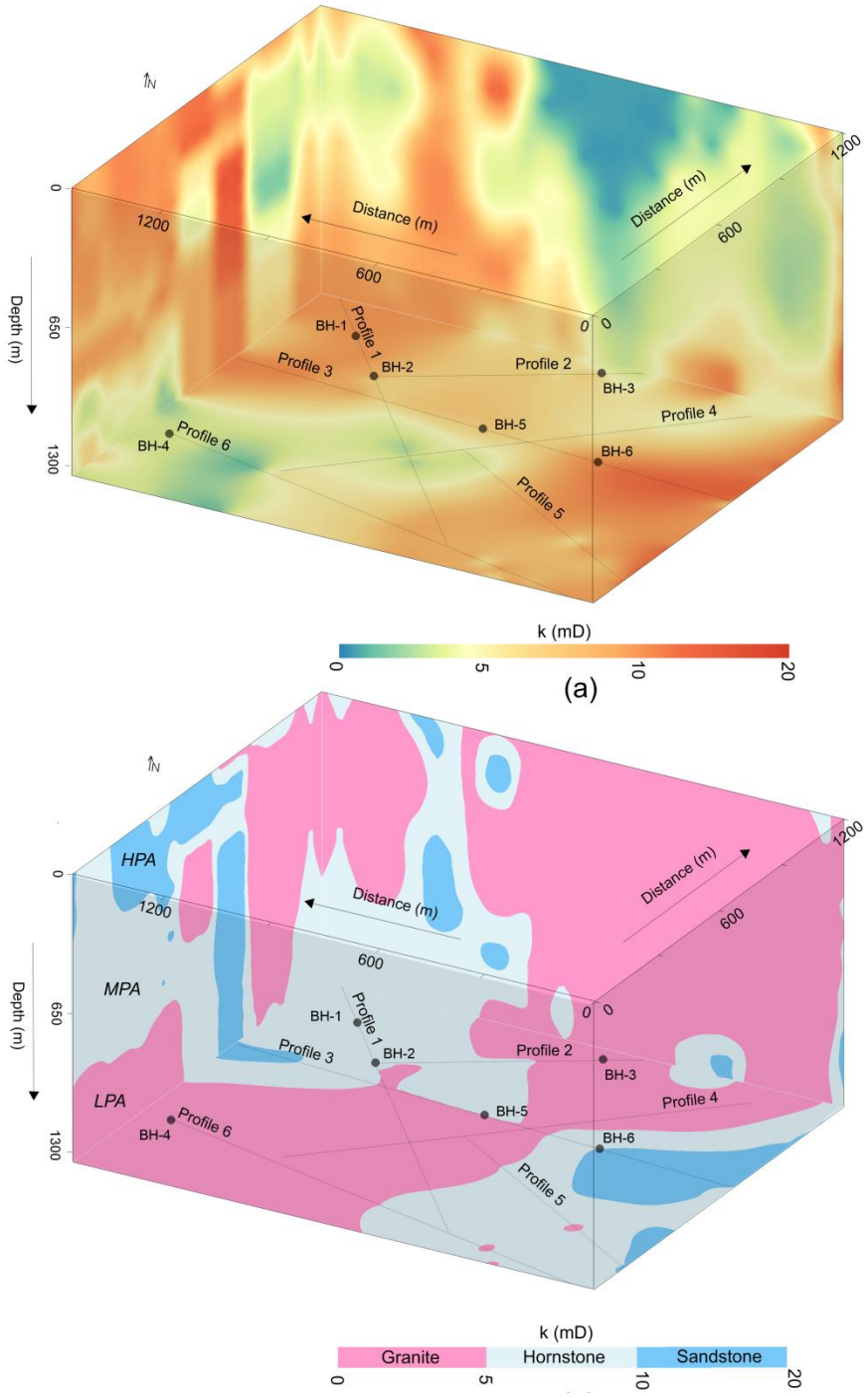

676

677 **Fig. 11.** The 3D k models, obtained from the correlation of CSAMT and borehole data (with k
678 represented on a color scale ranging from green to red), illustrate three groundwater potential aquifers:
679 low potential aquifer (LPA), medium potential aquifer (MPA), and high potential aquifer (HPA),

680 associated with three geological strata: granite, hornstone, and sandstone , respectively, for (a) the internal
681 view of the 3D k model, and (b) the analysis of the 3D (internal perspective) k model

682 **3.4 Depth-wise groundwater assessments**

683 Because of the scarcity of borehole data, it is not possible to use the observed k (borehole-based
684 k) to determine the water-bearing capacity of rock masses located below 200 m deep. The
685 evaluation of hard rock groundwater resources was made efficient, precise, and comprehensive
686 by creating a high link between drilling and CSAMT data. Because of this, k could be quickly
687 and accurately determined up to depths of 1300 m. From 2D/3D groundwater yield insights, we
688 were able to derive anticipated k values at 0, 200, 600, 1000, and 1300 m depths (Fig. 12).
689 Evaluation of groundwater at a depth of 1300 m was based on the following criteria: The
690 southwest and northeastern regions are assessed for granite, which constitutes over 45% of the
691 subsoil in low potential aquifer locations. Near the granite formation in the northwest and
692 southeast, we looked into hornstone, which comprised 40% of the medium potential aquifer. In
693 the eastern region, subsurface assessments were conducted on high-yield sandstone for over 15%
694 of the total. For groundwater evaluation at a depth of 1000 m, the following standards were
695 applied to understand the subsurface: The subsoil around the high potential aquifers in the
696 southeast consisted of 14% sandstone. Near the granite in the southeast and northwest areas, 38%
697 of the hornstone belonged to a medium potential aquifer. There were three boundaries, in the
698 middle, to the northeast, and to the southwest, in the subsurface, which was 52% granite and had
699 a poor aquifer yield. We examined the hydrogeological conditions at 600 m below ground using
700 the following criteria: in the central and northern areas, a low-yielding granite aquifer constituted
701 55% of the subsurface; hornstone in the west part was more common, accounting for 32% of the
702 subsurface and indicating a medium-yielding aquifer; and in the southeastern regions, sandstone

was the most studied, constituting 13% of the subsoil and indicating a high-yielding aquifer. To assess the hydrogeological conditions at a depth of 200 m, the following criteria were used: Granite with a low potential aquifer constituted 64% of the total in the center and northern parts. Hornstone with a medium yield aquifer comprised 26% of the underground in the southern regions. Research in the west focused on sandstone that made up 10% of the subsoil and had a high potential aquifer. Surface measurements taken at a depth of 0 m allowed us to determine the following hydrogeological conditions: While a medium potential aquifer is contained within 22% of the southwesterly surface's hornstone, and granite with 69% of the subsurface in the middle part. The sandstone, which is primarily located in the southwest, contains a high potential aquifer and is studied on 9% of the surface. Fig. 12 shows that as we descend then thickness of the granite from low yield aquifers decreases. Midway through, when depth drops to 600 to 700 m, groundwater conditions are at their worst. In the northwest, southeast, and southwest areas, there are rock masses that could represent aquifers, especially at depths lower than 700 m.

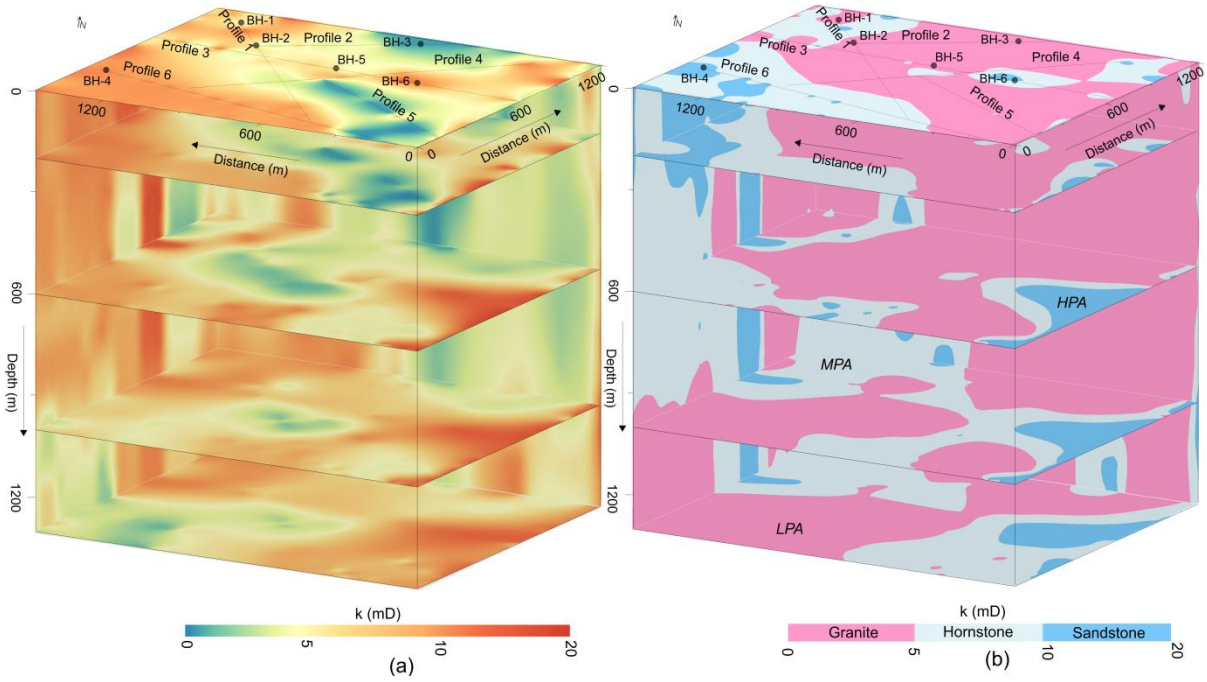

Fig. 12. (a) Geophysical permeability (k) imaging at depths of 0, 200, 600, 1000, and 1300 m, with k values represented on a color scale ranging from green to red. (b) Evaluation of CSAMT-derived k values (based on defined k ranges) at various depths for different aquifer types: low potential aquifer (LPA) in granite, medium potential aquifer (MPA) in hornstone, and high potential aquifer (HPA) in sandstone

3.5 Validation of predicted vs. measured permeability

Groundwater evaluations across the study area benefit significantly from the precise and systematic estimation of water-bearing capacity derived from CSAMT-based permeability (k). As shown in Fig. 6–12, granite dominates the central, northeastern, and southwestern zones, while hornstone, commonly classified as a type of metamorphosed sandstone, appears predominantly in the southeastern, western, and northwestern regions. Sandstone is extensively characterized in the eastern zones, with more limited data coverage in the west. Accurate assessment of groundwater potential using only borehole data is challenging due to inconsistencies in subsurface geological mapping. While drilling-based k values align with CSAMT-predicted k at select points around 200 m depth near boreholes, spatial extrapolation remains uncertain across larger areas. This mismatch underscores the difficulty of reliably assessing aquifer properties based solely on sparse drilling, especially in complex lithological settings.

Table 2 summarizes the percentage agreement between measured (drill-based) and predicted (CSAMT-based) k values. Agreement was evaluated by comparing matched depth intervals for each borehole–sounding pair using Eq. (4). For instance: BH-1 paired with P1-5 shows matching percentages of 73%, 63%, and 100% at depths of 10 m, 40 m, and 170 m, respectively. BH-2 and P1-9 exhibit matches of 80%, 77%, and 85% at 20 m, 60 m, and 185 m depths. BH-3 with P2-3 yields lower agreement: 67%, 40%, and 30% at 10 m, 85 m, and 200 m

depths. BH-4 and P6-1 show strong correspondence with 70%, 86%, and 78% at 15 m, 100 m, and 180 m depths. BH-5 and P3-15 demonstrate high agreement of 80%, 94%, and 85% at 30 m, 135 m, and 200 m depths. BH-6 and P3-21 produce matches of 61%, 74%, and 71% at 45 m, 165 m, and 180 m depths, respectively.

These results reveal a generally high degree of consistency between observed and predicted k values, with discrepancies likely arising from local heterogeneities or measurement uncertainties. Notably, even when the %match is low, the k values from both methods tend to classify the location into the same aquifer potential zone (low, medium, or high), reinforcing the reliability of the CSAMT-based approach for broader regional assessments.

Table 2

Percentage match and deviation between drilling-derived permeability (k) and CSAMT-derived permeability (k') for 18 selected data points out of the total 116

CSAMT data points (selected)			Drilling data			%Matching	Difference
CSAMT sounding number	Resistivity (Ωm)	Predicted k' using Eq. (4)	Borehole name	Depth (m)	Measured k	k' vs k	between k' and k
P1-5	392	7.0	BH-1	10	9.6	73	2.6
P1-5	515	5.5	BH-1	40	8.7	63	3.2
P1-5	1080	1.8	BH-1	170	1.8	100	0.0
P1-9	669	4.0	BH-2	20	5.0	80	1.0
P1-9	863	2.7	BH-2	60	3.5	77	0.8
P1-9	1354	1.02	BH-2	185	1.2	85	0.18
P2-3	2187	0.2	BH-3	10	0.3	67	0.1

P2-3	2988	0.04	BH-3	85	0.1	40	0.06
P2-3	4765	0.003	BH-3	200	0.01	30	0.007
P6-1	50	13.9	BH-4	15	19.9	70	6.0
P6-1	200	10.3	BH-4	100	12.0	86	1.7
P6-1	348	7.7	BH-4	180	9.9	78	2.2
P3-15	792	3.3	BH-5	30	4.1	80	0.8
P3-15	1157	1.5	BH-5	135	1.6	94	0.1
P3-15	1412	0.91	BH-5	200	1.07	85	0.16
P3-21	165	11.1	BH-6	45	18.2	61	7.1
P3-21	708	3.7	BH-6	165	5.0	74	1.3
P3-21	846	2.8	BH-6	180	2.0	71	0.8

4 Discussion

The integration of geophysical methods into groundwater research has gained significant traction in recent years, offering scalable and cost-effective alternatives to traditional drilling. While borehole investigations remain the most direct method for assessing permeability (k), they are often constrained by high costs, logistical complexity, and limited spatial coverage, particularly in deep, geologically heterogeneous terrains. Our study presents a novel and reliable framework for indirect 2D and 3D permeability modeling to depths exceeding 1 km, achieved by integrating CSAMT with borehole-derived data in a lithologically complex setting. This methodology addresses critical hydrogeological challenges in our study area, where surface water resources are limited and shallow granite exhibits low permeability. By contrast, deeper fractured granite, hornstone, and sandstone formations demonstrate significantly greater groundwater potential.

764 The resulting deep aquifer characterizations are aligned with China's national water security
765 initiatives and provide valuable input for sustainable groundwater management in the context of
766 increasing water stress and climate variability. Building on this foundation, our previous research
767 (Hasan and Shang, 2022; Hasan et al., 2025) applied similar geophysical strategies in
768 geotechnical engineering, where 2D and 3D modeling of Rock Quality Designation (RQD) and
769 rock mass integrity coefficient (Kv), two key geomechanical parameters, was conducted using
770 empirical correlations between borehole core data and resistivity derived from ERT/CSAMT.
771 These methods were instrumental in site evaluations for major national infrastructure projects,
772 including the Accelerator Driven System (ADS) in Huizhou and the Jiangmen Underground
773 Neutrino Observatory (JUNO), located approximately 700 m below ground in South Guangdong,
774 adjacent to the present study area. The successful deployment of this geophysical approach in
775 both hydrogeological and geotechnical domains underscores its reliability, scalability, and
776 interdisciplinary value for large-scale subsurface characterization.

777 CSAMT, introduced in the 1970s, remains uniquely valuable for deep subsurface
778 exploration, particularly in resistive, hard rock environments. Unlike conventional geophysical
779 techniques, CSAMT excels at delineating lithological boundaries and fluid-bearing zones.
780 Recent advances in instrumentation and inversion techniques have significantly enhanced its
781 resolution and depth penetration, enabling applications such as ours that extend its use beyond
782 historical limits. The novelty of this study lies not in the use of CSAMT or resistivity–
783 permeability relationships themselves, both of which are well-established, but in their integrated,
784 site-specific application to a geologically complex and deeply fractured hard rock environment
785 This is the first study to successfully model permeability at depths of up to 1300 m in granite,

786 sandstone, and hornstone using a data-driven approach validated by high-resolution borehole
787 data.

788 In this study, we established an empirical relationship between resistivity and
789 permeability using 116 co-located data pairs across the three dominant lithologies in the study
790 area: 62 for granite, 31 for sandstone, and 23 for hornstone. The dataset spans a resistivity range
791 of 35 to 4,765 Ωm and a permeability range of 0.01 to 19.9 mD, and is evenly distributed across
792 the geological formations, thereby minimizing lithological bias and ensuring robust calibration.
793 The derived correlation yielded a high coefficient of determination ($R^2 = 0.96$), indicating strong
794 predictive capability. The lithological classification emerging from this resistivity–permeability
795 relationship is both geologically consistent and empirically validated by field observations and
796 borehole data: low-permeability granite (>700 Ωm; k = 0–5 mD), moderate-permeability
797 hornstone (350–700 Ωm; k = 5–10 mD), and high-permeability sandstone (<350 Ωm; k = 10–
798 20 mD). These ranges reflect the distinct hydrogeological behavior of each unit under site-
799 specific geological conditions. We emphasize, however, that these resistivity–k associations are
800 localized and must be recalibrated for application in other regions with different geological
801 settings. The strength of our approach lies in its ability to significantly reduce the reliance on
802 extensive borehole drilling and direct permeability measurements, which are both cost-
803 prohibitive and operationally challenging, particularly in deep or structurally complex terrains.
804 By using a limited number of boreholes for calibration, our method enables the construction of
805 high-resolution 2D and 3D permeability models over large areas using CSAMT-derived
806 resistivity. If extensive borehole data were readily available or required, the added value of our
807 geophysical integration would diminish, along with its cost-effectiveness and broader
808 applicability. Thus, the novelty and practical relevance of our approach stem from its ability to

enhance subsurface characterization in data-scarce environments while minimizing invasive testing.

The fitted relationship between resistivity and permeability (k) in our study (shown in Fig. 5) is inherently influenced by several factors, including the geological setting, lithological variability, data distribution, and the accuracy of both resistivity and permeability measurements. The broad dynamic range observed in our dataset, resistivity values from 35 to 4,765 Ωm and permeability values from 0.01 to 19.9 mD, provides a solid foundation for resolving trends across all three dominant lithologies: sandstone, granite, and hornstone. This wide spread is particularly beneficial for characterizing high-resistivity rocks such as granite, where permeability remains consistently low and varies only slightly. In such cases, even large differences in resistivity correspond to minor changes in k, resulting in a smoother inverse trend. Conversely, in the lower resistivity range (e.g., <1500 Ωm) where permeability exceeds 1 mD, small changes in resistivity correspond to larger variations in k, resulting in a more scattered and nonlinear trend in the correlation. This behavior is expected and reflects real geological variability.

To ensure accuracy and reduce uncertainty, we implemented a robust workflow across all stages of data acquisition, processing, inversion, and modeling. For CSAMT, we employed careful survey design, optimized electrode configurations, and applied advanced filtering and static shift corrections. Inversion incorporated multidimensional modeling with borehole-constrained a priori information to improve resolution and reduce non-uniqueness. The permeability data from borehole cores were collected under controlled conditions, using high-quality, undisturbed samples from six boreholes, thereby reducing lab-to-field scale

discrepancies. These efforts, combined with integrated lithological data, yielded a reliable permeability model capable of informing groundwater assessments across the study domain.

Matching between measured and predicted permeability (k vs. k′) was also rigorously validated (Table 2). Among 18 selected points from boreholes, 10 showed a difference of less than 1 mD, with only two exceeding 4 mD. Despite minor deviations, all points were accurately classified by lithology. This confirms the empirical model's reliability and its utility for regional-scale k prediction, even in areas lacking direct measurements. The geophysical model effectively compensates for sparse drilling data, offering a scalable and cost-effective tool for hydrogeological evaluation in hard rock terrains.

While pumping tests provide average hydraulic conductivity over large volumes of subsurface material, making them suitable for establishing 1D correlation with spatially averaged geophysical data, they are less appropriate for high-resolution 2D or 3D modeling. In contrast, our objective was to develop detailed 2D and 3D permeability models that reflect the spatial heterogeneity of the subsurface. Achieving this level of resolution requires point-specific permeability measurements at varying depths, which align more precisely with the localized nature of resistivity values derived from CSAMT data. To meet this requirement, we employed rock core analysis rather than traditional pumping tests. Rock core testing offers the advantage of extracting permeability data at discrete depths and locations, providing a direct and fine-scale match with CSAMT-derived resistivity. This approach enhances the accuracy of the resistivity–permeability relationship and allows for more reliable permeability modeling in complex geological settings. Scale compatibility between CSAMT-derived resistivity and borehole-derived permeability (k) values was carefully addressed. The typical lateral resolution of

CSAMT (~50 × 50 meters) closely matches the spatial scale of the core-based permeability data used in this study.

Furthermore, our findings were cross-validated against existing geological data from both local and national surveys, revealing strong alignment with the established stratigraphy and hydrogeological characteristics of the region. This consistency reinforces the validity of our integrated geophysical–borehole approach, which offers a scientifically robust and practically scalable framework for estimating permeability in structurally complex and data-scarce terrains. While the methodology is rooted in established geophysical principles, the innovation of this study lies in its comprehensive, site-specific implementation, combining deep permeability modeling, field-based verification, and empirical calibration specifically tailored to the local geological context. Overall, the results underscore the considerable potential of geophysical techniques, particularly CSAMT, in supporting sustainable groundwater exploration and management at significant depths

5 Conclusions

This study presents an innovative, non-invasive approach to deep groundwater exploration using controlled-source audio-frequency magnetotellurics (CSAMT). For the first time, CSAMT has been applied to indirectly estimate two and three dimensional permeability (k) distributions in geologically complex hard rock terrains, extending to depths of up to 1300 m. While borehole drilling remains the conventional method for evaluating hydraulic parameters, it is often costly, logistically challenging, and limited in spatial coverage. Our approach significantly reduces reliance on boreholes while providing a more detailed and spatially extensive hydrogeological assessment. Using co-located CSAMT and borehole data, we developed a robust empirical

equation to estimate permeability based on resistivity values. This equation was applied across the study area to generate high-resolution k models that align closely with the known geology and stratigraphy. Specifically, sandstone, classified as a high potential aquifer (HPA), exhibited resistivity below 350 Ωm and permeability ranging from 10–20 mD. Hornstone, as a medium potential aquifer (MPA), showed resistivity between 350–700 Ωm and k values of 5–10 mD. Granite, representing a low potential aquifer (LPA), had resistivity above 700 Ωm with k ranging from 0–5 mD. These trends confirm the expected relationship between lower resistivity and higher permeability, validating the physical basis of our model.

Our 2D/3D permeability models further revealed that the most promising zones for deep groundwater occur in central regions below 700 m and around granite formations down to 1300 m. The close alignment between the modeled permeability and regional hydrogeological features highlights the reliability and predictive power of this method. By bridging the gap between sparse borehole data and robust hydrogeological models, CSAMT offers a cost-effective and scalable alternative for evaluating groundwater potential in hard rock regions. Looking forward, future research could enhance this method by refining the empirical models using broader hydrogeological datasets and integrating other geophysical parameters. This would deepen our understanding of the relationship between aquifer properties and geophysical signals, ultimately improving the reliability of groundwater assessments in challenging geological settings.

Code availability

Software application or custom code supports the published claims and complies with field standards

Data availability

Data available on request from the corresponding author

Author contributions

MH conceptualized the research goals and developed the methodology. MH and LS found the funding for the project. MH developed the code and prepared its visualization, and LS provided programming support and analysis tools. MH prepared the original draft.

Declaration of competing interest

The authors declare that they have no conflict of interest.

Acknowledgements

The authors wish to acknowledge the institutions that facilitated the research for this study: the State Key Laboratory of Mountain Hazards and Engineering Resilience, Institute of Mountain Hazards and Environment, Chinese Academy of Sciences, and China-Pakistan Joint Research Center on Earth Sciences, CAS-HEC, Islamabad, Pakistan.

Financial support

This research was financially supported by the National Natural Science Foundation of China's Research Fund for International Young Scientists (RFIS-I) (Grant No. 42350410442), and International Science and Technology Cooperation Program of Shanghai Cooperation Organization, Science and Technology Department, Xinjiang, China (Grant No. E202301005).

References

1. Abbas, M., Deparis, J., Isch, A., Mallet, C., Jodry, C., Azaroual, M., Abbar, B., and Baltassat, J.M.: Hydrogeophysical characterization and determination of petrophysical parameters by integrating geophysical and hydrogeological data at the limestone vadose zone of the Beauce aquifer, Journal of Hydrology, 615, 128725, 2022.
2. Allègre, V., Brodsky, E.E., Xue, L., Nale, S.M., Parker, B.L., and Cherry, J.A.: Using earth-tide induced water pressure changes to measure in situ permeability: A comparison with long-term pumping tests, Water Resour. Res, 52, 3113–3126, 2016.
3. Amiotte Suchet, P., Probst, J.L., and Ludwig, W.: Worldwide distribution of continental rock lithology: Implications for the atmospheric/ soil CO2 uptake by continental weathering and alkalinity river transport to the oceans, Glob Biogeochem Cycles, 17, 1038, 2003.
4. An, Z., and Di, Q.: Investigation of geological structures with a view to HLRW disposal, as revealed through 3D inversion of aeromagnetic and gravity data and the results of CSAMT exploration, Journal of Applied Geophysics, 135, 204–211, 2016.
5. Archie, G.E.: The electrical resistivity log as an aid in determining some reservoir characteristics, Transactions of the AIME, 146(1), 54–62, 1942.
6. Asfahani, J.: Estimation of the hydraulic parameters by using an alternative vertical electrical sounding technique: case study from semiarid Khanasser valley region Northern Syria, Acta Geophys, 71, 997–1013, 2023.
7. ASTM.: Standard Test Methods for Measurement of Hydraulic Conductivity of Saturated Porous Materials Using a Flexible Wall Permeameter (ASTM D5084-21), ASTM International, 2021.

8. Bai, D., Unsworth, M., Meju, M., Ma, X., Teng, J., Kong, X., Sun, Y., Sun, J., Wang, L., Jiang, C., Zhao, C., Xiao, P., and Liu, M.: Crustal deformation of the eastern Tibetan plateau revealed by magnetotelluric imaging, Nature Geosci., 3, 358–362, 2010.
9. Bear, J.: Dynamics of Fluids in Porous Media. Elsevier, 1972.
10. Bentley, L.R., and Gharibi, M.: Two- and three-dimensional electrical resistivity imaging at a heterogeneous remediation site, Geophysics, 69, 674–680, 2004.
11. Binley, A., and Kemna, A.: DC resistivity and induced polarization methods, In Hydrogeophysics, Springer, pp. 129–156, 129 2005.
12. Borah, U.K., and Patro, P.K.: Estimation of the depth of investigation in the magnetotelluric method from the phase, Geophysics, 84 (6), E377–E385, 2019.
13. Brace, W.F., Walsh, J.B., and Frangos, W.T.: Permeability of granite under high pressure, Journal of Geophysical Research, 73(6), 2225–2236, 1968.
14. Cagniard, L.: Basic theory of the magneto-telluric method of geophysical prospecting, Geophysics, 18 (3), 605–635, 1953.
15. Camporese, M., Cassiani, G., Deiana, R., and Salandin, P.: Assessment of local hydraulic properties from electrical resistivity tomography monitoring of a three-dimensional synthetic tracer test experiment, Water Resources Research, 47 (12), 2011.
16. Carbillet, L., Griffiths, L., Heap, M.J., Duwiquet, H., Baud, P., Violay, M.E.S., Reuschlé, T., and Guillou-Frottier, L.: The Influence of Micro- and Macrocracks on the Permeability of Granite, Rock Mech Rock Eng, https://doi.org/10.1007/s00603-024-04174-0, 2024.
17. Carman, P.C.: Flow of Gases through Porous Media, Butterworths Scientific Publications, 1956.

18. Clennell, M.B.: Tortuosity: a guide through the maze, Geological Society, London, Special Publications, 122(1), 299–344, 1997.
19. Courtois, N., Dewandel, B., Bhuvana, V., Ahmed, S., and Chandra, S.: Contribution of vertical and horizontal fractures to the groundwater flow in crystalline hard rock aquifers: Insights from a comparative study of three different sites in southern India, Hydrogeology Journal, 18(8), 1811–1827, 2010.
20. De Lima, O.A.L., and Niwas, S.: Estimation of hydraulic parameters of shaly sandstone aquifers from geological measurements, J Hydrol, 235, 12–26, 2000.
21. Dell'Oca, A., Guadagnini, A., and Riva, M.: Interpretation of multi-scale permeability data through an information theory perspective, Hydrol. Earth Syst. Sci., 24, 3097–3109, 2020.
22. Dewandel, B., Lachassagne, P., Wyns, R., Maréchal, J.C., and Krishnamurthy, N.S.: A generalized 3-D geological and hydrogeological conceptual model of granite aquifers controlled by single or multiphase weathering, Journal of Hydrology, 330(1–2), 260–284, 2006.
23. Di, Q., Fu, C., An, Z., Wang, R., Wang, G., Wang, M., Qi, S., and Liang, P.: An application of CSAMT for detecting weak geological structures near the deeply buried long tunnel of the Shijiazhuang-Taiyuan passenger railway line in the Taihang Mountains, Engineering Geology, 268, 105517, 2020.
24. Esmaeilpour, M., Ghanbarian, B., Sousa, R., Peter, R., and King, P.R.: Estimating Permeability and Its Scale Dependence at Pore Scale Using Renormalization Group Theory, Water Resources Research, 59 (5), e2022WR033462, 2023.

25. Faybishenko, B., Witherspoon, P.A., and Benson, S.M.: Fracture-matrix interaction in unsaturated fractured rock: Experimental observations and modeling, Journal of Contaminant Hydrology, 46(3–4), 223–256, 2000.
26. Ferguson, G., McIntosh, J.C., Jasechko, S., Kim, J.H., Famiglietti, J.S., and McDonnell, J.J.: Groundwater deeper than 500 m contributes less than 0.1% of global river discharge, Communication Earth and Environment, 4, 48, 2023.
27. Fernando, A., and Pacheco, L.: Regional groundwater flow in hard rocks, Science of the Total Environment, 506–507, 182–195, 2015.
28. Fiandaca, G., Maurya, P.K., Balbarini, N., Hördt, A., Christiansen, A.V., Foged, N., Bjerg, P.L., and Auken, E.: Permeability estimation directly from logging-while-drilling induced polarization data, Water Resources Research, 54, 2851–2870, 2018.
29. Fu, C., Di, Q., and An, Z.: Application of the CSAMT method to groundwater exploration in a metropolitan environment, Geophysics, 78 (5), 201–B209, 2013.
30. Fusheng, G., Haiyan, Y., Zengqian, H., Zhichun, W., Ziyu, L., Guocan, W., Linfu, X., Ye, G., and Wanpeng, Z.: Structural setting of the Zoujiashan-Julong'an region, Xiangshan volcanic basin, China, interpreted from modern CSAMT data, Ore Geology Reviews, 150, 105180, 2022.
31. Gerke, H.H., Dusek, J., and Vogel, T.: Mass transfer effects in 2-D dual-permeability modeling of field preferential bromide leaching with drain effluent, Hydrol. Earth Syst. Sci. Discuss., 8, 5917–5967, 2011.
32. Gleeson, T., Moosdorf, N., Hartmann, J., and van Beek, L.P.H.: A glimpse beneath earth's surface: Global hydrogeology maps (GLHYMPS) of permeability and porosity, Geophysical Research Letters, 43(2), 1–8, 2016.

33. Glover, P.W.J.: Geophysical properties of the near surface Earth: electrical properties, Treatise on Geophysics, 11, 89–137, 2015.
34. Hasan, M., Su, L., Cui, P., and Shang, Y.: Development of deep-underground engineering structures via 2D and 3D RQD prediction using non-invasive CSAMT, Scientific Reports, 15, 1403, 2025.
35. Hasan, M., and Shang, Y.: Geophysical evaluation of geological model uncertainty for infrastructure design and groundwater assessments, Engineering Geology, 299, 106560, 2022.
36. Hasan, M., Shang, Y., Jin, W., and Akhter, G.: Estimation of hydraulic parameters in a hard rock aquifer using integrated surface geoelectrical method and pumping test data in southeast Guangdong China, Geosci J, 25 (2), 223–242, 2021.
37. Hsieh, P.A., Neuzil, C.E., and Bredehoeft, J.D.: Flow tests in the crystalline rocks of the Whiteshell Research Area, Manitoba, Canada, Water Resources Research, 17(2), 496–504, 1981.
38. Hu, X.Y., Peng, R.H., Wu, G.J., Wang, W.P., Huo, G.P., and Han, B.: Mineral exploration using CSAMT data: application to Longmen region metallogenic belt, Guangdong Province, China, Geophysics, 78, B111–B119, 2013.
39. Hubbard, S.H., and Rubin, Y.: Hydrogeological parameter estimation using geophysical data: a review of selected techniques, J Contam Hydrol, 45 (3), 34, 2002.
40. ISRM.: Suggested methods for determining the permeability of rocks, International Society for Rock Mechanics, 2007.

41. Jardani, A., Revil, A., Dupont, J. P., and Benderitter, Y.: Detection of preferential groundwater pathways in sinkhole fields using self-potential methods, Journal of Hydrology, 335(1–2), 187–199, 2007.
42. Jasechko, S., Seybold, H., Perrone, D., Fan, Y., Shamsudduha, M., Taylor, R.G., Fallatah, O., and Kirchner, J.W.: Rapid groundwater decline and some cases of recovery in aquifers globally, Nature, 625, 715–721, 2024.
43. Jiang, Y., Wu, X., and Shi, Z.: A novel model to estimate permeability from formation resistivity, Journal of Petroleum Science and Engineering, 124, 15–23, 2014.
44. Kouadio, K.L., Liu, R., Malory, A.O., and Liu, C.: A novel approach for water reservoir mapping using controlled source audio-frequency magnetotelluric in Xingning area, Hunan Province, China, Geophysical Prospecting, 71, 1708–1727, 2023.
45. Lachassagne, P., Wyns, R., and Dewandel, B.: The fracture permeability in hard rocks aquifers and its dynamic modeling: An integrated conceptual model of weathered crystalline aquifers, Hydrogeology Journal, 29(1), 1–20, 2021.
46. Laghari, A.N., Vanham, D., and Rauch, W.: The Indus basin in the framework of current and future water resources management, Hydrology and Earth System Sciences, 16 (4), 1063–1083, 2012.
47. Lin, C.H., Lin, C.P., Hung, Y.C., Chung, C.C., Wu, P.L., and Liu, H.C.: Application of geophysical methods in a dam project: Life cycle perspective and Taiwan experience, Journal of Applied Geophysics, 158, 82–92, 2018.
48. Liu, X., Zhang, Y., and Zhang, D.: Permeability characteristics of fractured granite under varying stress conditions, Rock Mechanics and Rock Engineering, 54(3), 937–952, 2021.

49. Majumdar, R.K., and Das, D.: Hydrological characterization and estimation of aquifer properties from electrical sounding data in Sagar Island region, South 24 Parganas, West Bengal, India, Asian J Earth Sci, 4, 60–74, 2011.
50. Margat, J., and van der Gun, J.: Groundwater around the world: A geographic synopsis. CRC Press, 2013. https://doi.org/10.1201/b13977.
51. McKeown, C., Haszeldine, R.S., and Couples, G.D.: Mathematical modelling of groundwater flow at Sellafield, UK. Engineering Geology, 52(3–4), 231–250, 1999.
52. Medici, G., Ling, F., and Shang, J.: Review of discrete fracture network characterization for geothermal energy extraction, Frontiers in Earth Science, 11, 1328397, 2023.
53. Mira Geoscience Ltd.: GOCAD Mining Suite 3D Geological Modeling Software. Nancy University, Lorraine, France, 1999.
54. MOHURD (Ministry of Housing and Urban-Rural Development of the People's Republic of China).: National Groundwater Resources Strategic Survey and Planning Guidelines (in Chinese). Beijing: China Geological Press, 2021.
55. Mudunuru, M.K., Cromwell, E.L.D., Wang, H., and Chen, X.: Deep learning to estimate permeability using geophysical data, Advances in Water Resources, 167, 104272, 2022.
56. Neuzil, C.E.: How permeable are clays and shales? Water Resources Research, 30(2), 145–150, 1994.
57. Niu, G., Chen, M., and Fan, L.: Stress-dependent permeability of fractured granite and its implications for enhanced geothermal systems, Geothermics, 64, 294–303, 2016.
58. Niwas, S., and De Lima, O.A.L.: Aquifer parameter estimation from surface resistivity data, Groundwater, 41, 94–99, 2003.

59. Nwosu, L.I., Nwankwo, C.N., and Ekine, A.S.: Geoelectric investigation of the hydraulic properties of the aquiferous zones for evaluation of groundwater potentials in the complex geological area of imostate, Nigeria, Asian J Earth Sci, 6, 1–15, 2013.
60. Paterson, M.S., and Wong, T.F.: Experimental Rock Deformation: The Brittle Field, Springer, 2005.
61. Pellet, H., Arfib, B., Henry, P., Touron, S., and Gassier, G.: Mesoscale permeability variations estimated from natural airflows in the decorated Cosquer Cave (southeastern France), Hydrol. Earth Syst. Sci., 28, 4035–4057, 2024.
62. Phoenix Geophysics CMTPro, The Canadian Phoenix CMT Pro Version software for CSAMT data processing. Toronto, Ontario, Canada, 2020.
63. Phoenix Geophysics CSAMT-SW, The Canadian Phoenix CSAMT-SW Version software for CSAMT data inversion. Toronto, Ontario, Canada, 2020.
64. Qian, H., Wang, Y., Zhang, Y., and Su, Y.: Advances in deep groundwater exploration and management under climatic stress in arid regions of China, Journal of Hydrology, 626, 130234, 2024.
65. Qin, X.: Application of Unwedge program to geological stability analysis of deep buried deposits, Comprehensive, 8, 270–273, 2017 (In Chinese)
66. Refsgaard, J.C., Arnbjerg-Nielsen, K., Drews, M., Halsnæs, K., Jeppesen, E., Madsen, H., and Christensen, J.H.: The role of uncertainty in climate change adaptation strategies – A Danish water management example, Mitigation and Adaptation Strategies for Global Change, 18(3), 337–359, 2012.
67. Revil, A., and Cathles, L.M.: Permeability of shaly sands, Water Resources Research, 35(3), 651–662, 1999.

68. Roa-García, M.C., Brown, S., Schreier, H., and Lavkulich, L.M.: The role of land use and soils in regulating water flow in small headwater catchments of the Andes, Water Resources Research, 47(5), 2010.
69. Robinson, J., Slater, L., Johnson, T., Shapiro, A., Tiedeman, C., Ntarlagiannis, D., Johnson, C., Day-Lewis, F., Lacombe, P., Imbrigiotta, T., and Lane, J.: Imaging pathways in fractured rock using three-dimensional electrical resistivity tomography, Groundwater, 54 (2), 186–201, 2016.
70. Rodell, M., Velicogna, I., and Famiglietti, J.S.: Satellite-based estimates of groundwater depletion in India, Nature, 460 (7258), 999–1002, 2009.
71. Rodi, W., and Mackie, R.L.: Nonlinear conjugate gradients algorithm for 2-D magnetotelluric inversion, Geophysics, 66 (1), 174–187, 2001.
72. Simpson, F., and Bahr, K.: Practical magnetotellurics. Cambridge University Press, Cambridge. 254 pp, 2005.
73. Singh, K.P.: Nonlinear estimation of aquifer parameters from surficial resistivity measurements, Hydrology and Earth System Sciences Discussions, 2 (3), 917–938, 2005.
74. Singh, R., Prasad, M., and Al-Tahini, A.: A comparative study of electrical and hydraulic properties in carbonate and siliciclastic rocks, Geophysical Journal International, 221(3), 1837–1855, 2020.
75. Sinha, R., Israil, M., and Singhal, D.C.: A hydrogeological model of the relationship between geoelectric and hydraulic parameters of anisotropic aquifers, Hydrogeol J, 17, 495–503, 2009.

76. Smith, J.T., and Booker, J.R.: Rapid inversion of two-and three-dimensional magnetotelluric data, Journal of Geophysical Research: Solid Earth, 96 (B3), 3905–3922, 1991.
77. Soupios, P.M., Kouli, M., Vallianatos, F., Vafidis, A., and Stavroulakis, G.: Estimation of aquifer hydraulic parameters from surficial geophysical methods: a case study of Keritis Basin in Chania (Crete–Greece), J Hydrol, 1, 122–131, 2007.
78. Vouillamoz, J.M., Lawson, F.M.A., Yalo, N., and Descloitres, M.: The use of magnetic resonance sounding for quantifying specific yield and transmissivity in hard rock aquifers: the example of Beni, J Appl Geophys, 107, 16–24, 2014.
79. Wada, Y., Van Beek, L.P., Van Kempen, C.M., Reckman, J.W., Vasak, S., and Bierkens, M.F.: Global depletion of groundwater resources, Geophysical Research Letters, 37 (20), 2010.
80. Wang, R., Yin, C., Wang, M., and Di, Q.: Laterally constrained inversion for CSAMT data interpretation, Journal of Applied Geophysics, 121, 63–70, 2015.
81. Wang, W., Xie, X., Zhang, Y., Yang, J., and Liu, C.: Hydrogeological properties of fractured sandstones in southern China, Hydrogeology Journal, 22(5), 1127–1142, 2014.
82. Waxman, M.H., and Smits, L.J.M.: Electrical conductivities in oil-bearing shaly sands, Society of Petroleum Engineers Journal, 8(02), 107–122, 1968.
83. Webring, M.W.: MINC: A Gridding Program Based on Minimum Curvature: U.S. Geological Survey Open File Report, 81–1224, p. 41p, 1981.
84. Worthington, S.R.H., Davies, G.J., and Alexander, E.C. Jr.: Enhancement of bedrock permeability by weathering, Earth-Sci Rev, 160, 188–202, 2016.

85. Wynn, J., Mosbrucker, A., Pierce, H., and Spicer, K.: Where is the hot rock and where is the ground water-using CSAMT to map beneath and around Mount St. Helens, Journal of Environmental and Engineering Geophysics, 21, 79–87, 2016.
86. Yadav, G.S., and Singh, S.K.: Integrated resistivity surveys for delineation of fractures for ground water exploration in hard rock areas, Journal of Applied Geophysics, 62 (3), 301–312, 2007.
87. Yan, Y., Ma, L., Qian, J., Zhao, G., Fang, Y., Ma, H., and Wang, J.: Estimating permeability of rock fracture based on geometrical aperture using geoelectrical monitoring, Journal of Hydrology, 644, 132067, 2024.
88. Yang, H.Q., and Zhang, L.: Bayesian back analysis of unsaturated hydraulic parameters for rainfall-induced slope failure: A review, Earth-Science Reviews, 251, 104714, 2024.
89. Yang, J., Zhang, H., and Cui, Z.: Stability Analysis and Countermeasures of Rock Block in Underground Cavern, Guangdong Water Resources and Hydropower 5, 23–27, 2021 (In Chinese)
90. Zhang, F., Zhou, Z., Huang, Y., and Chen, Z.: Determining the Permeability of Fractured Rocks Based on Joint Mapping, Groundwater, 42, 509–515, 2004.
91. Zhang, J., Sirieix, C., Genty, D., Salmon, F., Verdet, C., Mateo, S., Xu, S., Bujan, S., Devaux, L., and Larcanché, M.: Imaging hydrological dynamics in karst unsaturated zones by time-lapse electrical resistivity tomography, Science of the Total Environment 907, 168037, 2024.
92. Zhang, L., Yang, C., and Qin, S.: Evaluation of groundwater flow in granite using core-based permeability and fracture analysis, Journal of Hydrology, 585, 124775, 2020.

93. Zhang, M., Farquharson, C.G., and Li, C.: Improved controlled source audio-frequency magnetotelluric method apparent resistivity pseudo-sections based on the frequency and frequency–spatial gradients of electromagnetic fields, Geophysical Prospecting, 69, 474–490, 2021.

94. Zhao, Y., Xu, T., and Luo, G.: Statistical analysis of rock permeability variation in different lithologies, Engineering Geology, 239, 123–133, 2018.

95. Zhu, L., Gong, H., Dai, Z., Guo, G., and Teatini, P.: Modeling 3-D permeability distribution in alluvial fans using facies architecture and geophysical acquisitions, Hydrol. Earth Syst. Sci., 21, 721–733, 2017.

96. Zonge, K.L., and Hughes, L.J.: Electromagnetic Methods—Theory and Practice, 1988.